Computational studies of collective effects in particle beams in the Future Circular Collider

Nico Klinkenberg

A thesis for the
Bachelor of Science
in
Applied Electrical Engineering

Westphalian University of Applied Sciences
First Examiner: Professor Doctor Peter Nalbach
Second Examiner: Doctor Sergey Arsenyev (CERN)

21. August 2018

Abstract

The conceptual design report **(CDR)** for the Future Circular Collider - hadron hadron **(FCC-hh)** is in its final stage to be presented to the European Strategy for Particle Physics Update in 2019. There are still open questions. One of these questions is whether the current stabilization program is sufficient to stabilize the beam. In this study, the stabilization effect of this scheme has been audited for the latest impedance model of the FCC-hh with two computational Vlasov solvers: Discrete-Expansion-Over-Laguerre-Polynomials-and-Head-Tail-Modes **(DELPHI)** and Nested Head-Tail **(NHT)**.
After introducing basic concepts to analyze the beam stability, a theoretical background for these two Vlasov solvers will be described.
Then a sufficient transverse feedback setting is proposed for injection and top energy. A bottleneck in the impedance of the FCC-hh and a destabilizing effect of strong resistive transverse feedback at top energy is also revealed.
In addition, a comparison to an analytical approach (Sacherer formalism) is given, and it is exposed why this equation cannot be applied for the FCC-hh parameters.

Keywords: FCC-hh, Beam instabilities, CDR, Collective effects, Octupoles, Transverse feedback, Wake fields, Impedance, TMCI, Destabilizing of strong resistive transverse feedback, Sacherer formalism

Acknowledgements

I feel truly honored that I was allowed to work in recent months under the leadership of a brilliant scientist, such as Sergey Arsenyev. By his clear explanations, he introduced me to the world of particle accelerator physics within a short time and sharpened my eye for the essential.

Furthermore, I am especially indebted to Daniel Schulte, my CERN supervisor, for making all this possible in the first place.

I would like to express my gratitude to Peter Nalbach, my university supervisor. In the last years of my work for him, I was allowed to learn an incredible amount, and his door was, for all kinds of questions and suggestions, never closed.

Not to forget my office colleagues and friends, Ryan Bodenstein and Kyle Poland. Excited discussions with them have significantly improved the quality of this work.

I would also like to thank everyone who contributed directly or indirectly to this work and the ABP group members in general, with whom I felt welcome instantly from day one.

Contents

List of Figures

List of Tables

Introduction

Motivation of the FCC-hh study

The Large-Hadron-Collider **(LHC)** design was launched in 1983. After that decision, it took 26 years to achieve the first run of the LHC. Already in 2013, the European Strategy for Particle Physics requested the investigation of a possible Post-LHC-collider which could be hosted at the Conseil Européen pour la Recherche Nucléaire **(CERN)**.
The Future Circular Collider **(FCC)** study has been launched in 2014 which is a merge of the highest-energy, highest-luminosity large circular colliders studies LEP3/TLEP and VHE-LHC. The current study considers a circular collider with a circumference of 97.75 km and includes three different designs. There is the FCC-ee for an electron-electron collision with a center-of-mass energy of 90-365 GeV. The FCC-he for a proton-electron collision that would collide a 60 GeV electron beam and a 50 TeV proton beam and the FCC-hh which is a proton-proton collider and provides a center-of-mass collision of 100 TeV. Some key parameters from the FCC-hh and the LHC are compared in Table 1. The FCC-hh layout is shown in Figure 1a and consists of two high luminosity experiments at A and G, two other smaller experiments and injection at L and B, collimation at J, momentum cleaning at F, extraction at D and, H houses the radiofrequency system [16, 14].

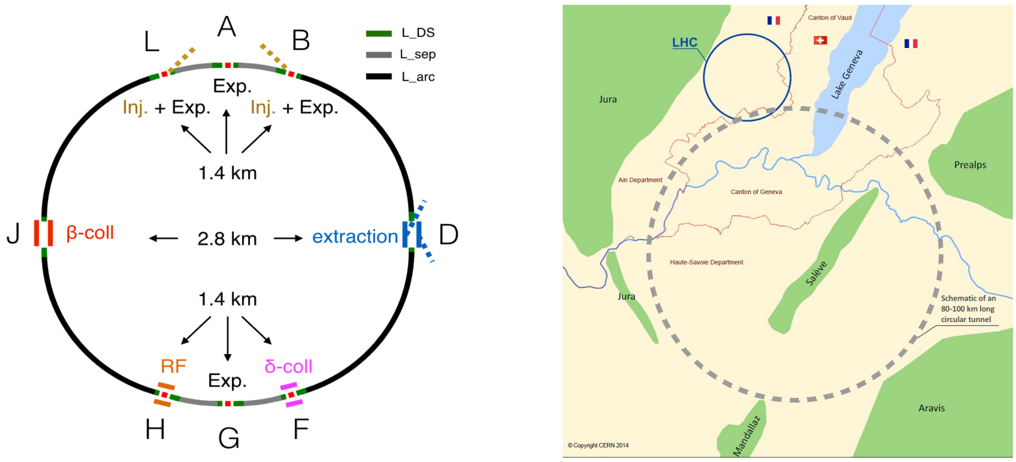

(a) FCC-hh layout

(b) FCC-hh placed in the Geneva area

Figure 1: Basic layout of the FCC [14]

parameter	unit	LHC	FCC-hh
centre-of-mass energy	TeV	14	100
injection energy	TeV	0.45	3.3
arc dipole field	T	8.33	16
circumference	km	26.7	97.8
beam current	A	0.58	0.5
bunch population N_b	10^{11}	1.15	1.0
number of bunches/beam	-	2808	10600

Table 1: Comparision of a few LHC and FCC-hh key parameter [14]

Motivation of this beam stability study for FCC-hh

Collective effects

The term collective effects comprises the interaction of several particles with each other. The way of interaction can be patterned into

- space charge effects, particles in a beam push each other away
- beam-beam effects, the different beams in the collider affect each other in the interaction regions
- wake fields/impedance, beam interacts with its environment

Facing high beam energies, the space charge effect becomes less important than the two other ones. The beam-beam effects are studied separately. This study will focus on the interactions of the beam with its surroundings. This is a crucial aspect of the design, as it limits the number of particles in the beam before the collective effects create bunch instabilities that destroy the beam.

Landau Octupoles

An octupole is a magnet which applies a nonlinear force to a particle with respect to its variance from the design orbit.
Therefore they can damp the coherent transverse beam instabilities caused by collective effects by providing a spread in tune. This spread in tune leads to a stabilizing mechanism called Landau damping. One usually refers to octupoles as passive stabilization elements [20].

Transverse feedback system

A transverse feedback system is a part of an accelerator that is meant to stabilize the transverse beam motion on its trajectory around the accelerator.
It uses a beam-screen-monitor to capture the displacement of the bunch to produce an electric signal. The signal is then processed by the transverse feedback system electronics and forwarded to a kicker magnet which applies a correcting force to the beam. Transverse feedback systems are usually referred to as active stabilization elements.

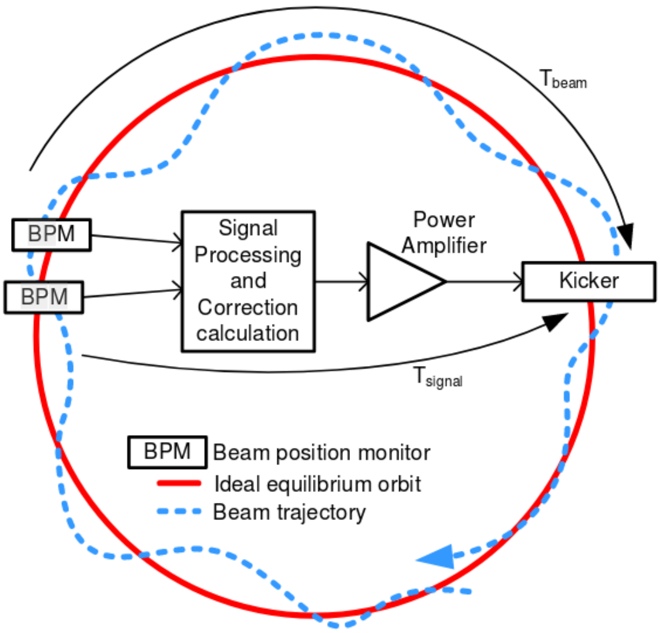

Figure 2: Sketch of a transverse feedback [12]

Conceptual Design Report

The FCC collaboration is currently focusing on the completion of the conceptual design report **(CDR)**. This report must be finished by the end of the year and will be presented to the next European Strategy for Particle Physics Update in 2019. Given the size of the budget for this project, various proofs of concept must be provided [16, 14, 8].
One of these aspects is the transverse beam stability. In the LHC the transverse feedback system together with the octupoles scheme has been sufficient to provide stabilization of the beam. In the FCC, the stabilizing effect of octupoles will be less effective, as it is proportional to the inverse of the squared relativistic gamma factor of the beam. However, the FCC will use stronger octupoles and more of them, which should almost cancel out the first effect. The actual assumption for the FCC-hh transverse stabilization scheme is that the transverse feedback system damps head-tail azimuthal mode 0 sufficiently while octupoles are used to support the transverse feedback system regarding all other modes. A full analysis for this stabilization scheme needs to be executed, and it has to be verified that this scheme works for injection and top energy, otherwise alternatives like for example **(e.g.)** stronger octupoles, electron lenses, radio frequency quadrupoles or a technique called "collide and squeeze" need to be considered [19]. The analysis has been performed in depth with two computational Vlasov solvers called DELPHI and Nested Head-Tail and is presented in this thesis.

Chapter 1

Basic concepts for beam stability studies

In this chapter, basic concepts concerning beam stability studies are presented. First of all, the conventional accelerator coordinate system, essential values concerning accelerators, and differential equations to describe the particles on their way around the design orbit under the influence of different forces are introduced. The second part will explain the concept of wake fields and impedance which are used to describe the interaction between the beam and its surroundings. Finally, a brief overview of the different oscillation modes in the beam is given.

1.1 The trajectories of the particles

In Figure 1.1 the conventional coordinate system is shown. A virtual particle trajectory is going to be taken as a reference for all others. Whereas older resources parametrize the motion via time, one can choose the speed of the virtual particle to be constant and conventionally uses the arc length variable s instead, which is related to the time t via $s = vt$ [10].
A distortion in the longitudinal direction is going to be described by the variable z, a horizontal displacement in the transverse plane by x and a vertical one in the transverse plane by y.
Therefore, we get a six-coordinate vector $\left(x, x', y, y', z, \frac{\Delta p}{p}\right)$ to describe the motion of the particle. The derivatives are with respect to s and $\frac{\Delta p}{p}$ is the relative momentum error of the particle [9, p.8].

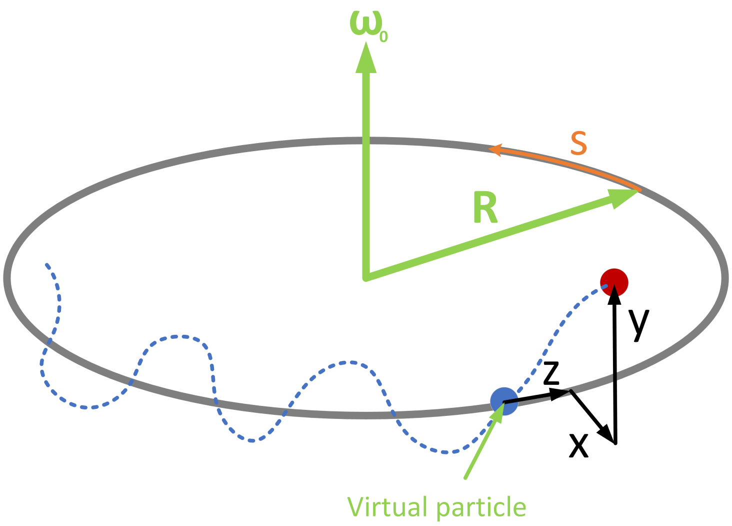

Figure 1.1: Sketch of the conventional accelerator coordinate system

1.1.1 Equations of motion and phase space ellipse

Along its way on the orbit the single particle underlies different forces. In the most accessible model, these forces are at least the bending forces by the dipole magnets to provide a closed path around the orbit and the focusing forces by the quadrupoles to correct transverse displacement, e.g., caused by gravity. Therefore the following differential equations can be assumed to describe the particle orbit as a harmonic oscillator.

$$\frac{d^2x}{ds} + Kx = 0 \tag{1.1}$$

$$\frac{d^2y}{ds} + Ky = 0 \tag{1.2}$$

K is a factor that is defined by the force of the magnets. If the force that is applied to the particle would be constant with s, then the equation of motions would become

$$x = A\cos(\frac{\omega}{v}s + \phi), \tag{1.3}$$

$$x' = -A\frac{\omega}{v}\sin(\frac{\omega}{v}s + \phi). \tag{1.4}$$

There is a problem with this assumption because in a real accelerator K cannot be considered to be constant. It varies with respect to the variable s. Therefore the Equations 1.1/1.2 need to be modified by writing $K(s)$ instead of K. Regarding the solution of the modified differential equations (called Hill equations), the following constant and variables need to be introduced:

- ϵ := transverse emittance
- $\beta(s)$:= the amplitude modulation
- $\Psi(s)$:= phase advance

The emittance ϵ is a constant that is defined by the injector chain. The area that is covered in the phase space by a bunch of particles is defined by $\epsilon\pi$. The amplitude modulation, also called betatron-function, and the phase advance both vary with the focusing strength.

For the multi-particle case, one needs to define how many particles are taken into account to define the covered area $\epsilon\pi$ in phase space. This value varies typically between 95 and 100 % [4][5, p.19].

$$x = \sqrt{\epsilon\beta(s)}\cos(\Psi(s) + \phi) \tag{1.5}$$

$$x' = \sqrt{\frac{\epsilon}{\beta(s)}}\sin(\Psi(s) + \phi) \tag{1.6}$$

Equation 1.5/1.6: Solution of Hill's differential equation

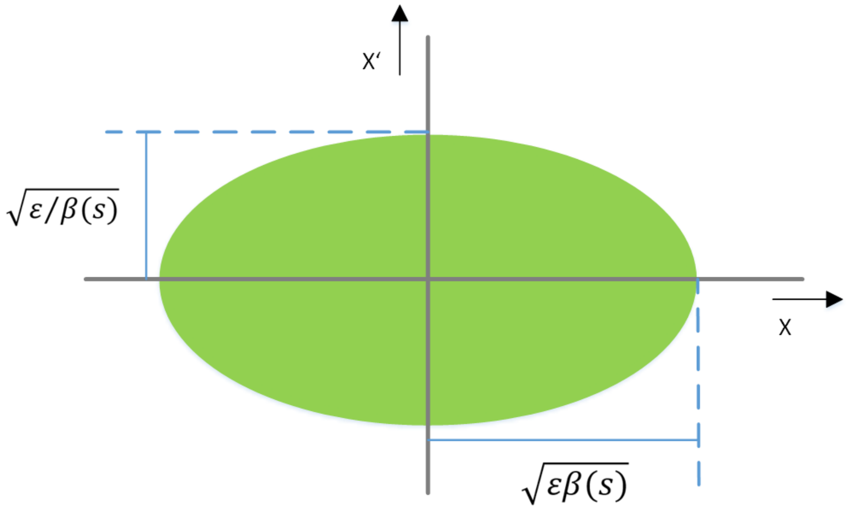

Figure 1.2: Phase space of particles

1.1.2 The tune shift

Using the smooth approximation in Equations 1.1/1.2, the tune Q is defined by

$$Q_{x0} = \frac{\omega_{x0}}{\omega_0}, \tag{1.7}$$

$$Q_{y0} = \frac{\omega_{y0}}{\omega_0}, \tag{1.8}$$

where $\omega_0 = v/R$ is the angular revolution frequency of the particle around the circular accelerator and $\omega_{x0,y0}$ is the angular revolution frequency in the transverse plane. Thereby the betatron tune Q can be depicted as the number of transverse revolutions per turn around the accelerator. Therefore the differential equation of the harmonic oscillator can be written as [9, p. 9]

$$x'' + \frac{Q_{x0}^2}{R^2}x = 0, \tag{1.9}$$

$$y'' + \frac{Q_{y0}^2}{R^2}y = 0. \tag{1.10}$$

In this model, no external perturbations are taken into account. If one now adds a perturbation into Equation 1.9, this equation can be written as

$$x'' + \left(\frac{Q_{x0}^2 - \chi R^2}{R^2}\right)x = 0, \tag{1.11}$$

where χ is a perturbation that is linear in x. As one can see from Equation 1.11 the squared resonant frequency has now been shifted by χ, and therefore we can rewrite the tune Q as

$$Q_x^2 = Q_{x0}^2 - \chi R^2. \tag{1.12}$$

For small perturbations one can define the complex coherent tune shift as [9, p. 12]

$$\Delta Q = Q_x - Q_{x0} = -\frac{\chi R^2}{2Q_{x0}}. \tag{1.13}$$

The equation of motion for the longitudinal plane is defined as

$$z' = -\eta\delta, \tag{1.14}$$

where η is the slippage factor and δ is the relative momentum error. The slippage factor η is defined as

$$\eta = \frac{1}{\gamma_t} - \frac{1}{\gamma}, \tag{1.15}$$

where γ_t is the transition gamma (an accelerator constant) and $\gamma = 1/\sqrt{1-(\frac{v}{c})^2}$. With these equations, one can calculate that a particle slows down if it is faster than the virtual particle and its momentum error is positive. This is caused by the fact that a particle needs to increase its orbit with increasing energy. The circulation time increases because it cannot accelerate anymore due to the fact that the particle is already close to the speed of light [9, p. 9].
The tune in the longitudinal direction s is called synchrotron tune Q_s and follows the definition of the tune from Equations 1.7/1.8.
Now a link between the longitudinal and transverse particle motion is introduced by introducing the chromaticity ξ quantifying the dependence of the tune on the momentum spread δ. [9, p.154][6, p.35]. The chromaticity is defined as

$$\xi = \frac{\Delta Q}{Q_0}/\delta = \frac{\Delta Q}{Q_0}/\frac{\Delta p}{p_0}, \tag{1.16}$$

where p_0 is the nominal particle momentum and Δp is the particle momentum deviation. To analyze the stability of a beam, it is crucial to calculate the complex coherent tune shift ΔQ. The tune can be shifted by electromagnetic fields that are caused by the interaction of parts of the accelerator like (dipoles, quadrupoles, RF cavities, beam-screen monitors) with the beam or by the beam itself. The concept of wake fields and impedance is used to study the influence of the different surroundings on the beam around the accelerator [1]. This is very crucial because there is a clash of interest. On the one side, the accelerator should be operated at high bunch intensity to detect more rare events which are measured in luminosity L. On the other hand, one may not drive these beam intensity to high to obtain stability and a longer beam lifetime. The luminosity L is defined as

$$L = \frac{n_b N^2 \gamma f_0}{4\pi\sigma_x\sigma_y}. \tag{1.17}$$

L is defined over the number of bunches n_b, the beam intensity N, the revolution frequency f_0, the relativistic gamma factor of the beam γ and the root mean square beam sizes σ_x and σ_y [1, p.1].

1.2 Wake fields and impedance

In this section, the concept of wake fields and impedance is exposed. This concept describes the interaction of the beam with its surroundings. The particles in high-energy accelerators like the LHC and the FCC are moving close to the speed of light, and therefore the image charges that a particle induces in a surrounding surface can interact with trailing particles.
The study of the wake fields is usually a demanding task, and it is mostly proceeded by numerical solving of the Maxwell equations for different shapes and conductivity of the surrounding surfaces. A general classification into two main contributors to the impedance can be made:

- Resistive wall impedance that is caused by the limited conductivity of the surrounding surfaces
- Geometric wall impedance that is caused by changes in the form of the surrounding surfaces [21]

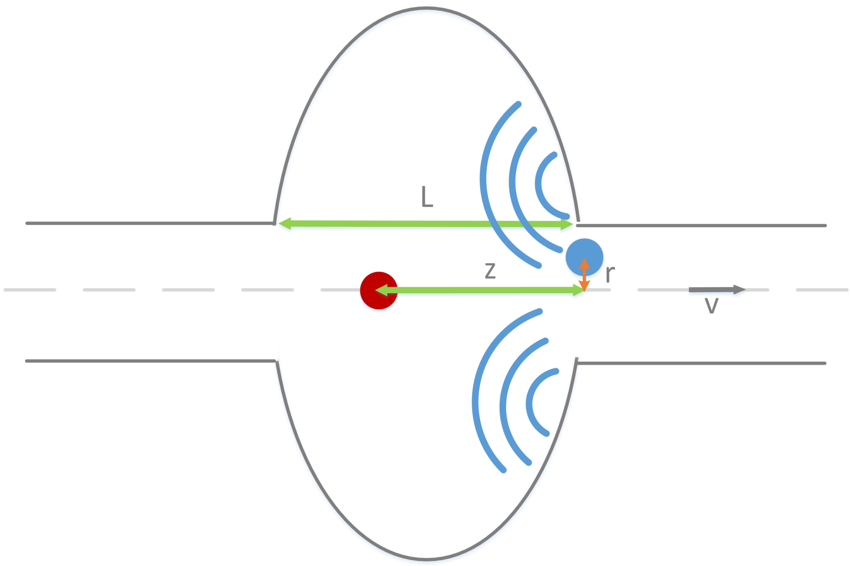

Figure 1.3: Geometric wake field caused by resonant cavity

In Figure 1.3, one can see the drive particle in blue which induces an image charge in the resonant cavity. This charge applies a perturbation force to the red witness particle while it travels through the resonant cavity. This force F makes its presence felt as [1, p.7]

- an energy gain (in J) $U(z) = \int_0^L F_{\parallel} ds$ in the longitudinal plane, which depends on the distance z between the two particles
- a torsional moment $r\vec{M}(z) = \int_0^L \vec{F}_{\perp} d\vec{s}$ in the transversal plane, with r as the transversal displacement to the design orbit

$U(z)$ and $M(z)$ are then normalized by the charge q and are going to be referred as wake functions

$$W_{\parallel}(z) = -\frac{U(z)}{q^2}, \tag{1.18}$$

$$\vec{W}_{\perp}(z) = \frac{\vec{M}(z)}{q^2}. \tag{1.19}$$

Due to the periodicity of circular colliders, it is often simpler to calculate in the frequency domain than in time domain. Therefore the wake functions are going to be Fourier transformed and are now referred to as impedances [3, p.50]

$$Z_{\parallel}(\omega) = \frac{1}{c}\int_{-\infty}^{\infty} W_{\parallel}(z)e^{\frac{j\omega z}{c}}dz, \tag{1.20}$$

$$\vec{Z}_{\perp}(\omega) = \frac{-j}{c}\int_{-\infty}^{\infty} \vec{W}_{\perp}(z)e^{\frac{j\omega z}{c}}dz. \tag{1.21}$$

Vertical impedance Equation 1.20 in Ω and the horizontal impedance Equation 1.21 in $\frac{\Omega}{m}$

1.3 Different types of instability modes

This work focuses on three different mode numbers that define the oscillations within the beam. First, there is the head-tail oscillation, which represents the oscillation within a structure of one bunch. This oscillation can be addressed by the azimuthal mode number l and the radial mode number n. The azimuthal mode number l defines the azimuthal structure of the area that is covered in the longitudinal phase space. The oscillation itself can be visualized as Figure 1.4 shows. For example, $l = 0$ is a complete transverse oscillation of a bunch, and a head-tail azimuthal $l = 1$ oscillation has a node in the middle of the bunch. The frequency of these head-tail azimuthal modes l is in the unperturbed case defined by $(Q_{x0,y0}\omega_0 + l\omega_s)$. Therefore the definition of the tune shift ΔQ for the head-tail modes have to be extended by the azimuthal mode number l such that we obtain

$$\Delta Q = \frac{\omega_{x,y} - \omega_{x0,y0} - l\omega_s}{\omega_0} = Q_{x,y} - Q_{x0,y0} - lQ_s. \tag{1.22}$$

All head-tail azimuthal modes contain a substructure of different head-tail radial modes. This radial mode n defines the radial structure of the beam in the longitudinal phase space.

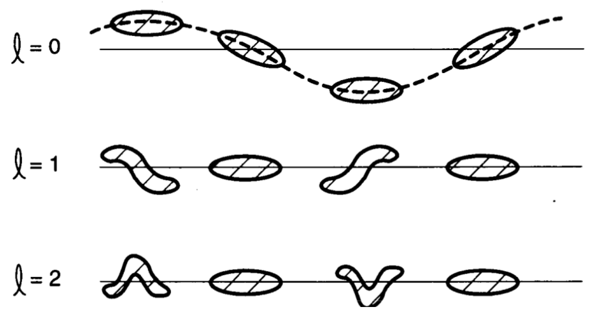

Figure 1.4: Sketch of a few beams for head-tail azimuthal l [9, p.270]

Furthermore, in this project more than one bunch will be studied. This leads to a third oscillation number. This third oscillation number is called coupled-bunch mode μ and defines the oscillation of all bunches as a beam. This can be visualized as Figure 1.5 shows.

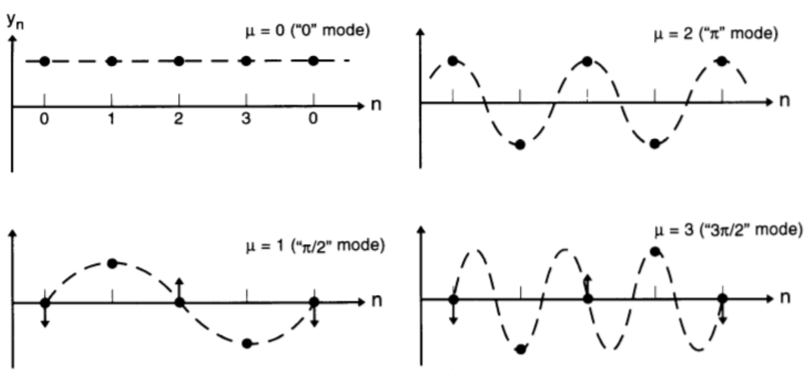

Figure 1.5: Snapshot patterns of the coupled-bunch mode μ for a beam with four bunches [9, p.206]

Chapter 2

Solving the Vlasov equation

This chapter will discuss the Vlasov equation which treats the beam like a collisionless plasma and has been shown to be sufficient to study the stability of particle beams. In modern accelerator physics, tracking codes are used which track every single particle on its own. The problem with this approach is that it becomes cumbersome to track every particle in a beam at high bunch intensity, especially when the multi-bunch case is studied. After introducing the Vlasov equation, the basic functionalities behind DELPHI and Nested Head-Tail **(NHT)** will be discussed.

2.1 Vlasov equation

Most of the following steps and definitions are taken from [15]. The Vlasov equation describes the time evolution of an ensemble of particles in phase space. It states that the phase space volume of an ensemble Ψ does not change over time if all forces are conservative. Hence, effects like, e.g., synchrotron radiation are excluded. Since protons are going to be used for this study, this assumption is okay. The equation is written as

$$\frac{d\Psi}{ds} = 0, \tag{2.1}$$

where s is the position on the circular design orbit. Since it is assumed that there will be no coupling between the transverse planes, a dependency can be neglected when studying one transverse plane. The following steps assume the analysis for the vertical plane y, but they are exactly the same for the horizontal plane x. Expanding the total derivative Equation 2.1 into partial ones leads to the following equation [9, p.276]

$$\frac{\partial\Psi}{\partial s} + y'\frac{\partial\Psi}{\partial y} + p_y'\frac{\partial\Psi}{\partial p_y} + z'\frac{\partial\Psi}{\partial z} + \delta'\frac{\partial\Psi}{\partial\delta} = 0. \tag{2.2}$$

The particle density Ψ is, as it stated in Equation 2.2, a function depending on the transverse position y and its momentum p_y as well as his longitudinal displacement z and the error in momentum δ. All derivatives, which are denoted by a prime, are with respect to the arc length s.
To simplify the upcoming calculation one may now change the transverse components displacement y and momentum p_y to another set of canonical variables. This transformation can be stated as [15, pp.9-10]

$$y = \sqrt{2J_y\frac{R}{Q_{y0}}}\cos(\theta_y), \tag{2.3}$$

$$p_y = \sqrt{2J_y \frac{Q_{y0}}{R}} \sin(\theta_y), \tag{2.4}$$

where R is the accelerator radius and Q_{y0} corresponds to the tune for the nominal accelerator parameters. Therefore the Vlasov equation 2.2 can now be written as

$$\frac{\partial \Psi}{\partial s} + J_y' \frac{\partial \Psi}{\partial J} + \theta_y' \frac{\partial \Psi}{\partial \theta_y} + z' \frac{\partial \Psi}{\partial z} + \delta' \frac{\partial \Psi}{\partial \delta} = 0. \tag{2.5}$$

The Hamiltonian for a single particle needs to be introduced as

$$H = \underbrace{\frac{Q_y}{R} J_y}_{\text{transverse part}} \underbrace{- \frac{1}{2\eta} \left(\frac{\omega_s}{\nu}\right)^2 z^2 - \frac{\eta}{2}\delta^2}_{\text{longitudinal part(linear)}} - \underbrace{\frac{y}{E} F_y(z,s)}_{\text{dipole wake fields}} . \tag{2.6}$$

In this equation, the wake force is represented by $F(z, s)$, the energy of the particle with E, the velocity of the particle by $\nu = \beta c$, ω_s is the synchrotron frequency, and η is the slippage factor. The canonical equations for Equation 2.6 are therefore expressed by

$$J_y' = -\frac{\partial H}{\partial \theta_y} = \frac{\partial y}{\partial \theta_y} \frac{F_y(z,s)}{E}, \tag{2.7}$$

$$\theta' = \frac{\partial H}{\partial J_y} = \frac{Q_y}{R} - \frac{\partial y}{\partial J_y} \frac{F_y(z,s)}{E}, \tag{2.8}$$

$$z' = \frac{\partial H}{\partial \delta} = -\eta\delta, \tag{2.9}$$

$$\delta' = -\frac{\partial H}{\partial z} = \left(\frac{\omega_s}{\nu}\right)^2 \frac{z}{\eta}. \tag{2.10}$$

If we now express Equation 2.5 with the canonical equation one gets [1]

$$\frac{\partial \Psi}{\partial s} + \frac{F_y(z,s)}{E} \frac{\partial y}{\partial \theta_y} \frac{\partial \Psi}{\partial J_y} + \left(\frac{Q_y}{R} - \frac{F_y(z,s)}{E} \frac{\partial y}{\partial J_y}\right) \frac{\partial \Psi}{\partial \theta_y} - \eta\delta \frac{\partial \Psi}{\partial z} + \left(\frac{\omega_s}{\nu}\right)^2 \frac{z}{\eta} \frac{\partial \Psi}{\partial \delta} = 0. \tag{2.11}$$

2.2 DELPHI

DELPHI is short for "Discrete Expansion over Laguerre Polynomials and HeadtaIl modes" and is a computational Vlasov solver. It takes the Sacherer integral equation, which is going to be derived from the Vlasov equation by a perturbation approach, and transforms it into an eigenvalue problem by expanding its solution over associated Laguerre polynomials.

Deriving the Sacherer integral equation

First, different separation ansatzes are made. One assumes a perturbation Ψ_1 developing on top of the reference distribution Ψ_0. Furthermore, the unperturbed distribution Ψ_0 is modeled to be only depending on J_y and r. This is sensible, since the unperturbed reference distribution can be set as a Gaussian and the corresponding uncoupled variables J_z and r can be interpreted as sort of phase space distances. For the same reasons of uncoupling between longitudinal and transverse variables, the perturbation Ψ_1 can be separated. Furthermore, the perturbation Ψ_1 oscillates with a complex frequency Ω that is defined as $\Omega = Q_c\omega_0$. The resulting perturbation approach can be written as

$$\Psi(s, J_y, \theta_y, z, \delta) = \underbrace{f_0(J_y)g_0(r)}_{\text{unperturbed distribution } \Psi_0} + \underbrace{f_1(J_y, \theta_y)g_1(z, \delta)e^{\frac{j\Omega s}{\nu}}}_{\text{perturbation } \Psi_1}. \tag{2.12}$$

As a next step, polar coordinates $\left(z = r\cos(\phi),\ \delta = \frac{\omega_s}{\eta\nu} r\sin(\phi)\right)$ are used to represent the longitudinal coordinates. This polar coordinates and the perturbation approach for Ψ are now inserted into the Vlasov equation 2.11 to end up with

$$\left(f_1 g_1 \frac{j\Omega}{\nu} + \frac{Q_y}{R} g_1 \frac{\partial f_1}{\partial \theta_y} + \frac{\omega_s}{\nu} f_1 \frac{\partial g_1}{\partial \phi}\right) e^{\frac{j\Omega s}{\nu}} = \frac{\sin(\theta_y)}{E}\sqrt{2J_y \frac{R}{Q_{y0}}} F_y(z, s) g_0(r) f_0'(J_y). \tag{2.13}$$

One can expand $g_1(r, \phi)$ into a Fourier series and approximate $f_1(J_y, \theta_y)$ as a simple dipole motion. Therefore these functions can be rewritten as

$$f_1(J_y, \theta_y) = f(J_y)e^{-j\theta_y}, \tag{2.14}$$

$$g_1(r, \phi) = e^{-\frac{jQ_y' z}{\eta R}} \sum_{l=-\infty}^{l=\infty} R_l(r)e^{-jl\phi}, \tag{2.15}$$

where l is the azimuthal mode number. Using these definitions, Equation 2.13 becomes

$$\sum_{l=-\infty}^{l=\infty} R_l(r)e^{-jl\phi}\left(\frac{f(J_y)(Q_c - Q_{y0} - lQ_s)}{f_0'(J_y)\sqrt{\frac{2J_y R}{Q_{y0}}}}\right) = \frac{R}{2E} F_y(z, s) e^{-j\frac{Q_c s}{R}} e^{-j\frac{Q_y' z}{\eta R}}. \tag{2.16}$$

Taking the equations for the wake force F_y from source [15, pp.25-35] into account, one can obtain the Sacherer integral equation which can be divided into a damper and an impedance part. The Sacherer integral equation is defined as

$$(\Omega - Q_{y0}\omega_0 - l\omega_s)R_l(\tau) = -\,\kappa g_0(\tau)\sum_{l'=-\infty}^{\infty} j^{l'-l}\int_0^\infty d\tau'\tau' R_{l'}(\tau') \underbrace{(\frac{\mu}{\omega_0}J_l(-\omega_\xi\tau)J_{l'}(-\omega_\xi\tau')}_{\text{damper term}} + \underbrace{\sum_{p=-\infty}^{\infty} Z_y(\omega_p)J_l((\omega_\xi-\omega_p)\tau)J_{l'}((\omega_\xi-\omega_p)\tau')).}_{\text{impedance term}} \tag{2.17}$$

To analyze the Sacherer integral equation one may find the following definitions helpful

$$\kappa = -j\frac{Nf_0e^2M}{2\gamma m_0 c Q_{y0}}, \tag{2.18}$$

$$\tau = \frac{r}{v}, \tag{2.19}$$

$$\omega_p = (\mu + pM + Q_{y0})\omega_0, \tag{2.20}$$

$$\omega_\xi = \frac{\xi O_{y0}\omega_0}{\eta}, \tag{2.21}$$

$$\eta = -j\frac{\omega_0^2}{2\pi\kappa n_d}, \tag{2.22}$$

where N is the intensity per bunch, M is the number of bunches, n_d is the number of damping turns, μ is the coupled-bunch mode, Z_y is the transverse impedance and J represents a Bessel function.

Expanding the Sacherer integral equation over Laguerre polynomials

To get a classical eigenvalue problem that can be solved numerically, the radial functions $g_0(\tau)$ and $R_l(\tau)$ are decomposed into Laguerre polynomials.

$$R_l(\tau) = (\frac{\tau}{\tau_b})^{|l|}e^{-b\tau^2}\sum_{n=0}^{\infty} c_n^l \underbrace{L_n^{|l|}(a\tau^2)}_{\text{Associated Laguerre polyn.}} \tag{2.23}$$

$$g_0(\tau) = e^{-b\tau^2}\sum_{k=0}^{n_0} g_k \underbrace{L_k^0(a\tau^2)}_{\text{Laguerre polyn.}} \tag{2.24}$$

Here, l represents the azimuthal mode number, n is radial mode number and k is an index. The Equations 2.23/2.24 can be inserted into the damper term such that one gets

$$\int_0^\infty \tau^{|l|+1}L_n^{|l|}(a\tau^2)e^{(b-a)\tau^2}g_0(\tau)J_l(\omega\tau)d\tau, \tag{2.25}$$

$$\int_0^\infty \tau^{|l|+1}L_n^{|l|}(a\tau^2)e^{-b\tau^2}J_l(\omega\tau)d\tau, \tag{2.26}$$

where a and b are convergence parameters that need to be adjusted by the user so that the impedance sum converges. In this study, a Gaussian longitudinal distribution is used where a and b are both set to 8.0 [15, p.39].

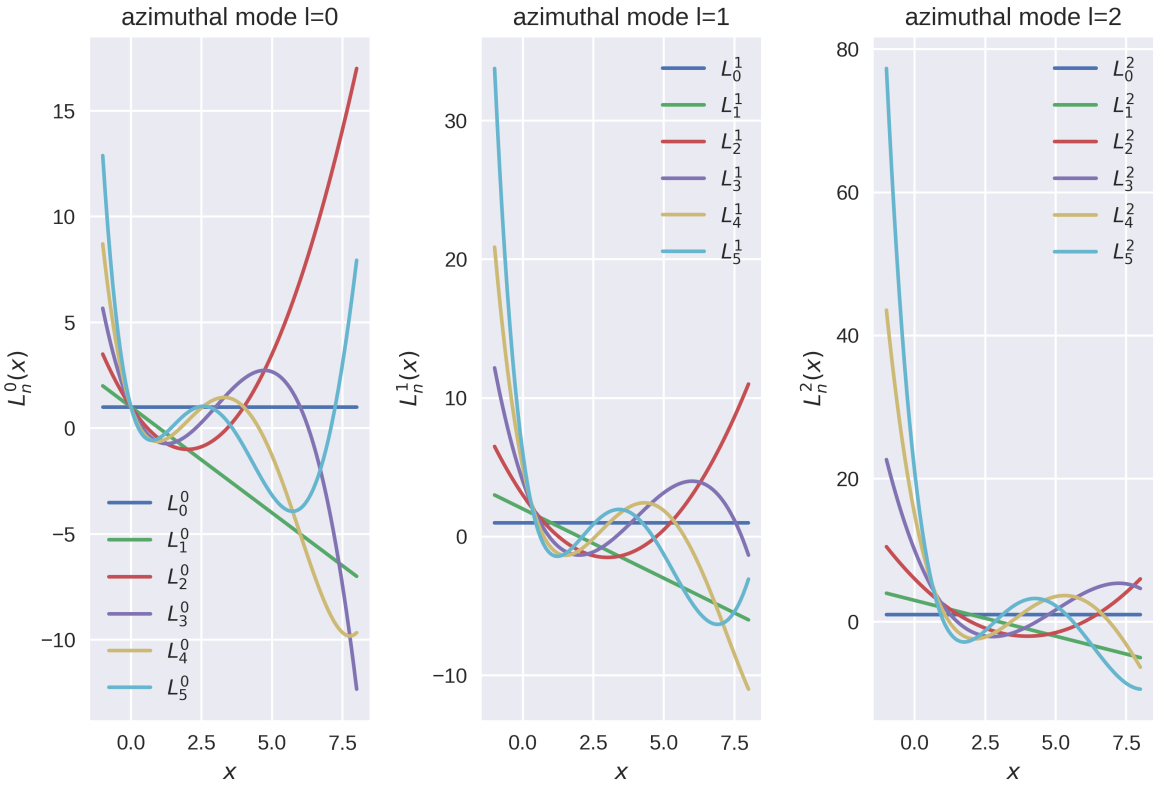

Figure 2.1: Associated Laguerre Polynomials for azimuthal modes $l = 0, 1, 2$

These two integrals can be computed numerically. Therefore the Sacherer integral Equation 2.17 can be written as

$$\underbrace{(\Omega - Q_{y0\omega 0})}_{\text{Eigenv. } \lambda} c_{n,l} = \sum_{l'}^{\infty} \sum_{n'}^{\infty} c_{n',l'} (\delta_{l,l'} \delta_{n,n'} l \omega_s + M_{l,n,l',n'}), \tag{2.27}$$

where n represents the radial mode number and the matrix M is a combination of the impedance and damper matrix. Since the single sums over the radial modes n and the azimuthal modes l diverge, the maximum number of calculated modes was set from 0 to 15 for the radial modes and from -16 to 16 for the azimuthal modes. DELPHI thereby solves the eigenvalue problem and returns the complex eigenvalue $(\Omega - Q_{y0}\omega_0)$ for each pair of radial and azimuthal modes (n, l).

2.3 Nested Head-Tail

Nested-Head-Tail **(NHT)** is a computational Vlasov solver like DELPHI. NHT uses an generalization of the air-bag model [9, p.338]. NHT defines a set of equipopulated nested rings in the longitudinal phase space and expands a set of head-tail harmonics Ψ_{in} on them to obtain a basis to describe the perturbation of the particle density. For example, a Gaussian distribution is then represented by a set of nested-air-bags as shown in Figure 2.2. This plot was created with NHT version written in Wolfram Mathematica for ten radial modes. The following explanations and equations are taken from article [7].

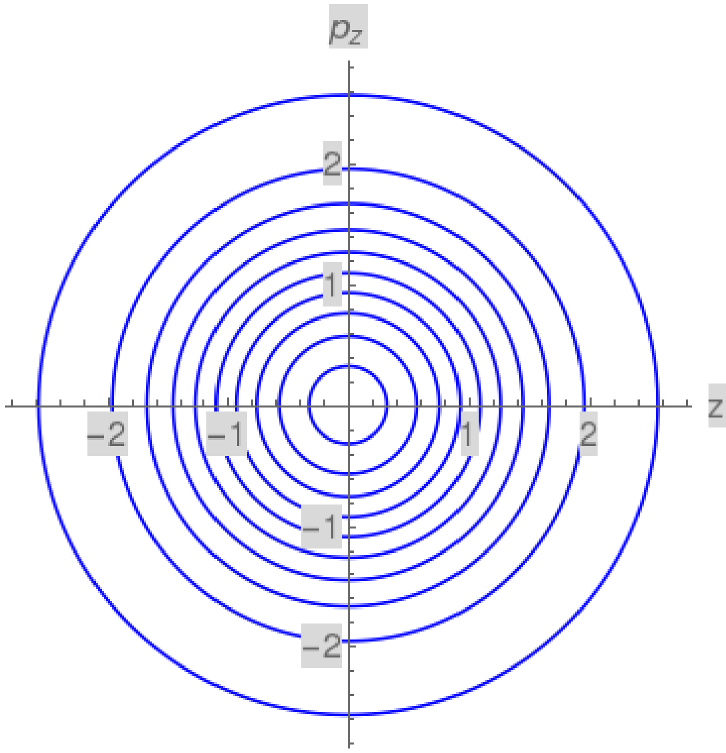

Figure 2.2: Set of nested-air-bags

The head-tail-harmonics Ψ_{ln} are defined as

$$\Psi_{ln} = e^{jl\phi + j\chi_n \cos(\phi) - jQ_x\omega_0 t}, \tag{2.28}$$

$$\chi = \frac{\xi Q_{x0}\omega_0 \tau_n}{\eta}, \tag{2.29}$$

where ϕ is the synchrotron phase, l is the azimuthal harmonic number, n represents the radial harmonic number, τ_n is the radii of the ring in phase space in time units, η is the slippage factor, Q_x is the tune in the trasnsverse plane, Q_{x0} is the unperturbed tune in the transverse plane and ξ is the chromaticity [6, p.35].
To solve a single bunch eigensystem one considers

$$\lambda X = \hat{S} \cdot X - j\hat{Z} \cdot X - jg\hat{F} \cdot X. \tag{2.30}$$

Here, X represents the perturbation vector defined in components of Ψ_{in}, $\hat{S}$ denotes the harmonic oscillations inside the RF potential well, $\hat{Z}$ is the impedance of the accelerator, g comprises the damper gain, and F represents a flat wake matrix.
They are defined as

$$\hat{S}_{lmn} = l\delta_{lm}\delta_{n\beta}, \tag{2.31}$$

$$\hat{Z}_{lmn\beta} = j^{l-m}\frac{\kappa}{n_r}\int_{-\infty}^{\infty} d\omega Z(\omega) J_l(\omega\tau_n - \chi_n) J_m(\omega\tau_\beta - \chi_\beta), \tag{2.32}$$

$$\kappa = \frac{N_b r_0 R_0}{8\pi^2\gamma Q_x Q_s}, \tag{2.33}$$

$$\hat{F}_{lmn\beta} = \frac{j^{m-l}}{n_r} J_l(\chi_n) J_m(\chi_\beta), \tag{2.34}$$

where $Z(\omega)$ represents the transverse impedance, N_b is the number of particles per bunch, r_0 is the classical radius, and R_0 is the radius of the accelerator. The eigenvalue $\lambda = \frac{\Omega}{\omega_s}$ rescales the coherent complex frequency in units of the synchrotron frequency ω_s.
For a multi-bunch eigensystem Equation 2.30 has to be extended by a term that represents the inter bunch-interaction. It is taken into account that all higher order modes are suppressed. Therefore a flat-wake matrix, similar to the steps done for the damper by $\hat{F}$, can be defined for the inter-bunch interaction. Hence, the eigensystem can be expanded as

$$\lambda X = \hat{S}\cdot X - j\hat{Z}\cdot X - jg\hat{F}\cdot X + \hat{C}\cdot X, \tag{2.35}$$

$$\hat{C} = 2\pi\kappa\hat{W}_\mu\hat{F}, \tag{2.36}$$

$$\tilde{W}_\mu = \sum_{k=1}^{\infty} W(-ks_0)e^{jk\phi_\mu}, \tag{2.37}$$

$$\phi = \frac{2\pi(\mu + Q_x)}{M}, \tag{2.38}$$

$$s_0 = \frac{2\pi R_0}{M}, \tag{2.39}$$

where μ represents the inter-bunch mode number, k is the bunch number and M is the number of bunches.

Chapter 3

Computational studies of collective effects

This chapter will discuss all the crucial issues that concern the stability studies of collective effects that have been performed with the two Vlasov solvers DELPHI and Nested Head-Tail. Both solvers have already been used for former studies at CERN's specialized group for Accelerator-Beam-Physics (**ABP**).
First, a general overview of the structure of procedure of this study is given. It will be explained what forms the input and output for this two Vlasov solvers and how we manage and separate the output. Then, a general overview of the input parameters used in this study is given. This is followed by a presentation and analysis of the obtained results. This contains the stabilizing transverse feedback setting, for injection energy as well as for top energy. After this, some other observed effects are going to be revealed, and a comparison to the Sacherer formalism for no feedback is also shown. The last part repeats the presentation of stabilizing transverse feedback settings for an impedance that has been improved because of some observations annotated in Section 3.4 in this study.
All scans have been performed for the vertical plane because the vertical impedance is worse than the horizontal impedance. Furthermore, we used a full resistive transverse feedback.

3.1 General annotations about this study

Input and output

For a better understanding of the next steps in this chapter, an overview of the general procedure to study the beam instability is given in Figure 3.1. The input parameters for a simulation are the impedance/wake function that defines the interaction of the beam with the parts of the accelerator and a set of different parameters, such as the number of bunches, number of particles per bunch, strength of the transverse feedback, chromaticity, the beam energy, and a lot more. For each of these combinations, one obtains a set of complex eigenvalues for every oscillation that is defined by the three mode numbers l, n, and μ. The head-tail mode numbers l and n are limited in DELPHI and NHT as Table 3.1 shows. NHT calculates all of these head-tail mode number combinations (l, n). DELPHI, on the other hand, stops automatically in accordance to convergence criteria, so that one may find less head-tail modes.

Vlasov Solver	max azimuthal modes	max rad. modes
DELPHI	-16 to 16	0 to 15
NHT	-10 to 10	0 to 10

Table 3.1: limits of head-tail modes

Both Vlasov solvers only keep the most unstable coupled bunch mode μ for every head-tail mode.

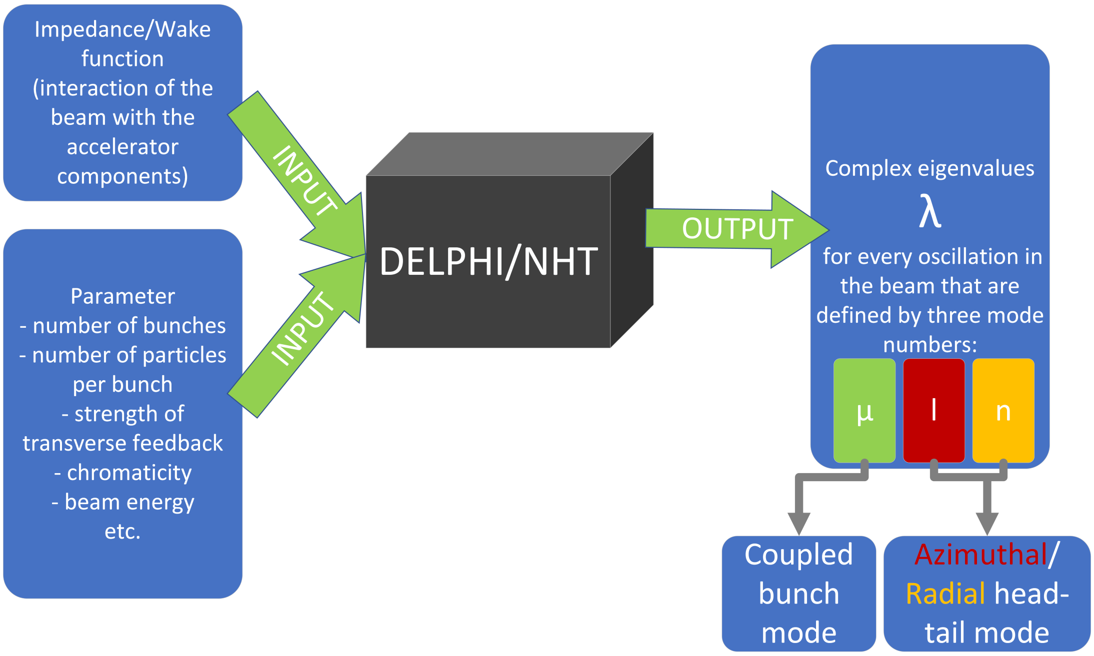

Figure 3.1: General procedure

These eigenvalues λ for every head-tail mode contain the information about their complex coherent frequency and can be written as

$$\lambda = \Omega - \omega_{y0}, \tag{3.1}$$

where Ω is the absolute complex coherent frequency of a head-tail mode and ω_{y0} is the angular revolution frequency of the virtual particle in the transverse plane. These eigenvalues are then used to obtain the tune shift and the growth rate of the modes as described below.

Obtaining tune shift and growth rate

It must be explained how to quantify the instability within a beam oscillation. Therefore one needs to make a connection between the eigenvalue and the complex coherent frequency shift $\Delta\omega$. They are connected by

$$\Delta\omega = \lambda - l\omega_s = \Omega - \omega_{y0} - l\omega_s, \tag{3.2}$$

where ω_s is the synchrotron frequency, and l is the azimuthal mode number assigned to each mode by the procedure described below. To clarify the connection between the different terms one may take a look at Figure 3.2. The real part tells by how much the frequency of this mode gets shifted because of the imaginary part of the impedance. The imaginary part tells how big the growth rate of this mode is due to the real part of the impedance. Therefore the most unstable mode has the most negative imaginary part.

$$\Delta\omega = \underbrace{Re(\Delta\omega)}_{\text{Shift of the frequency}} + j \underbrace{Im(\Delta\omega)}_{\text{Growth rate } -Im(\Delta\omega)=\frac{1}{\tau}} \tag{3.3}$$

In this study the complex coherent tune shift is also going to be used. It corresponds to the frequency shift and can be easily transformed as Equation 3.4, where ω_0 is the angular revolution frequency of the virtual particle around the accelerator.

$$\underbrace{\Delta Q}_{\text{complex coherent tune shift}} \omega_0 = \underbrace{\Delta\omega}_{\text{complex coherent frequency shift}} \tag{3.4}$$

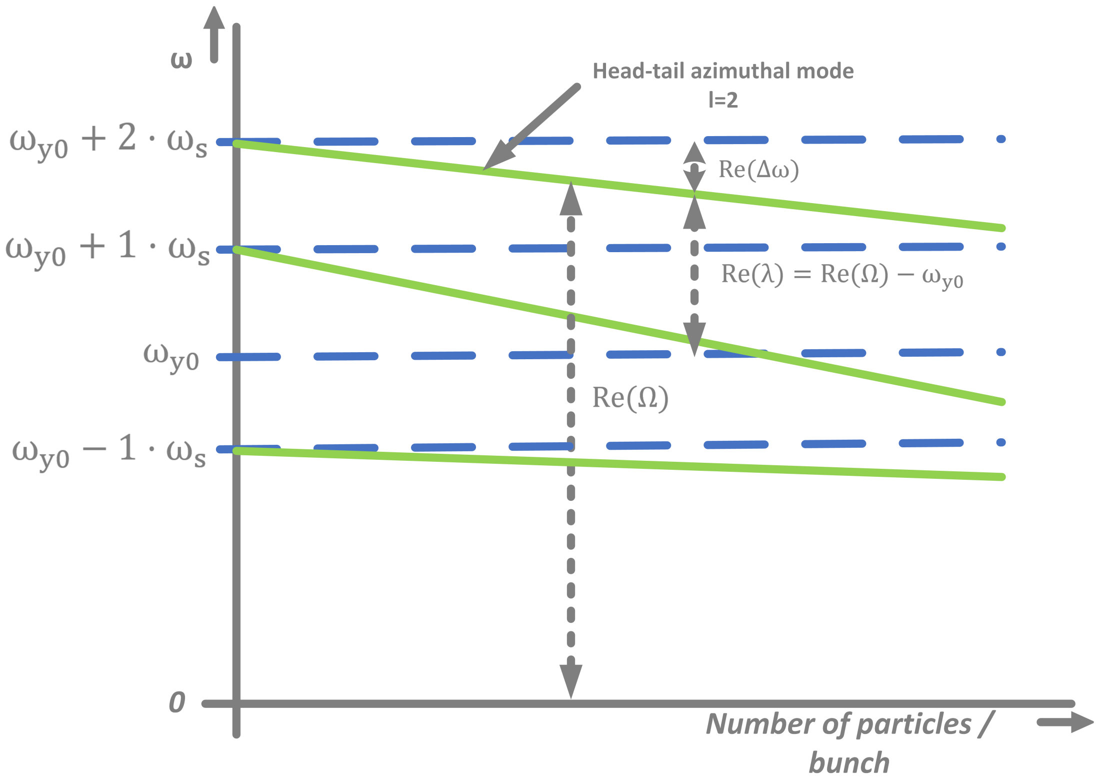

Figure 3.2: Clarification of the different angular frequency terms

Assigning head-tail mode numbers

Also one may like to know which exact head-tail mode (l, n) caused an instability. Unfortunately, neither Vlasov solver offers this option. With a little trick, it is still possible to obtain the information about the head-tail azimuthal mode l. If one takes a look at the definition

$$Re(\Omega) - \omega_{y0} = l\omega_s + Re(\Delta\omega), \tag{3.5}$$

it can be seen that the frequencies of the different modes differ by $l\omega_s$. Furthermore, $\Delta\omega$ is, in our simulations, negative or slightly positive so that we can separate the different head-tail azimuthal modes by solid ranges of $\omega_s\,(b + l))$ where b is a factor that varies between -85 % to 15 %. Unfortunately one cannot differentiate the different head-tail radial modes n that belong to a head-tail azimuthal mode l. Hence, we only keep the most unstable head-tail radial mode n within a head-tail azimuthal mode l.

Damping rate of transverse feedback

The term transverse feedback setting/damping rate needs to be explained. A damping rate of x turns quantifies the number of turns x that the transverse feedback system needs to annihilate a perturbation.

3.2 Impedance, accelerator, and octupole parameters

In this section, the most relevant input parameters for the simulations will be shown. The latest accelerator parameters are shown in Table 3.2. The only exception, in this case, is the number of bunches. In the FCC-hh around 80 % of the accelerator is going to be filled with bunches. The computational Vlasov solvers are not capable of simulating a partially filled accelerator. Therefore a uniform fill was used that fills 100 % of the accelerator. Hence, we are most probably overestimating the instabilities. Furthermore, the 13068 bunches fill 10 % of the available RF buckets as one can see from the harmonic number of 130680.

Accelerator parameter	Injection / Top energy
Beam energy / TeV	3.3 / 50
Bunch intensity / number of protons	10^{11}
Number of Bunches	13068
RMS bunch length σ_z / cm	8
4 RMS bunch length / ns	1.06741
Horizontal tune Q_x	111.28 / 109.31
Vertical tune Q_y	111.31 / 109.32
RF harmonic number h	130680
RF Voltage V / MV	12 / 32

Table 3.2: FCC-hh main parameters used in the studies [8]

The plots in Figure 3.3 show the latest dipolar impedance is shown. This includes all the crucial parts of the accelerator design [2][18]:

- Resistive wall of a cold beam screen (protection of the magnets from unstable particles)
- Amorphous carbon or titanium-nitride coating of the beam screen (suppression of e-clouds)
- Resistive wall of warm beampipe
- Collimators, resistive and geometrical impedance (cleaning of the beam halo)
- 400 MHz RF cavities (acceleration of the beam)
- Crab cavities (rotation of the bunch to maximize collisions at the interaction point)
- Interconnects between the cryomagnets

To obtain the full impedance, the single impedances of the different parts were weighted with their local beta-function and then summed up. The impedance at top energy is higher than at injection energy. This is mainly caused by the squeezed collimators. Furthermore, the β-function is small in the crab cavities at injection energy. This fact will become important in Section 3.4 again. These impedances exclude the beam position monitors and the injection kicker [18].

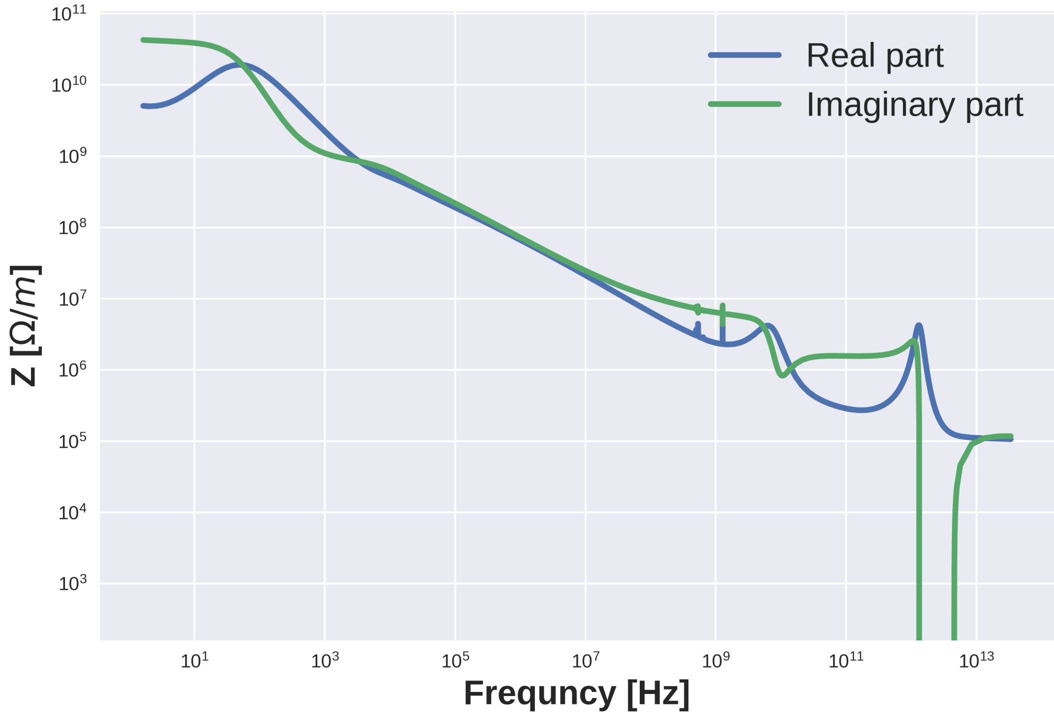

(a) Injection energy

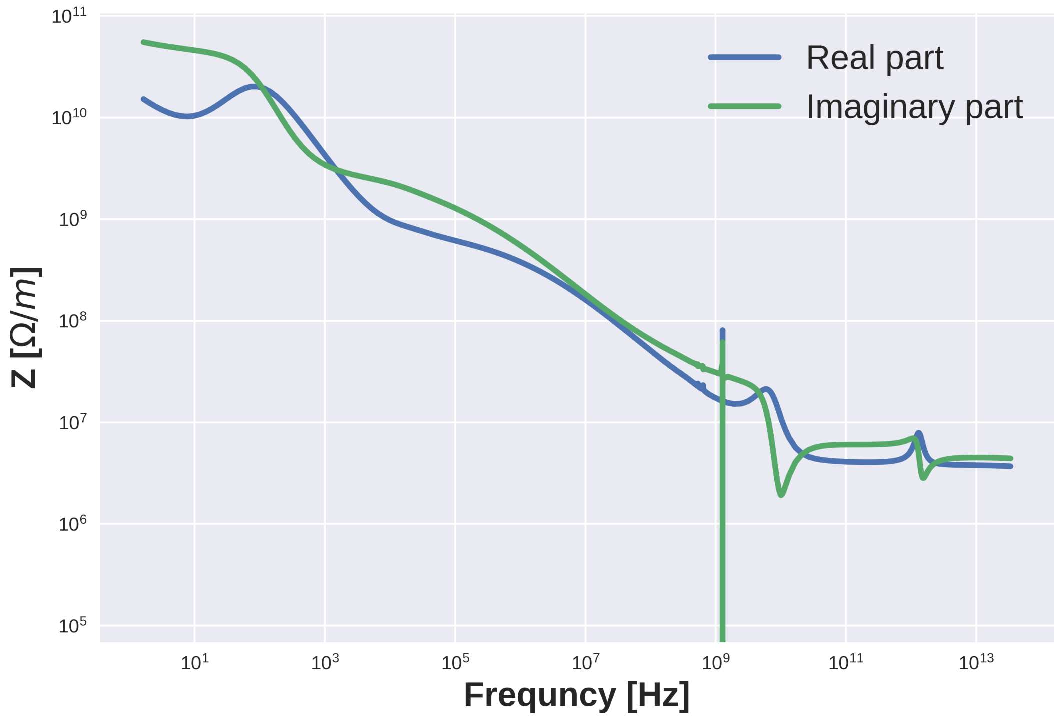

(b) Top energy

Figure 3.3: Vertical dipolar impedance as a function of frequency

Figure 3.4 shows the relative impedance distribution over the different elements at injection and top energy. The kHz range on the left side drives the coupled bunch instabilities while the GHz range on the right side drives single bunch instabilities. As already mentioned in the section before, the real part of the impedance drives the growth rates of the instabilities, and the imaginary part of the impedance causes the shift of the mode frequency. Looking at Figure 3.4, one can note that at injection and top energy, the coupled bunch instabilities are dominated by the beam screen. The single bunch instabilities at injection energy are driven by various elements like the beam screen, the collimators, and the interconnects. Furthermore, it is interesting to see that the coating of the beam screen has a significant influence on the frequency shift. At top energy, the growth rate and the tune are dominated by the collimators. As it was already mentioned above, this is caused because of the squeezed collimator settings.

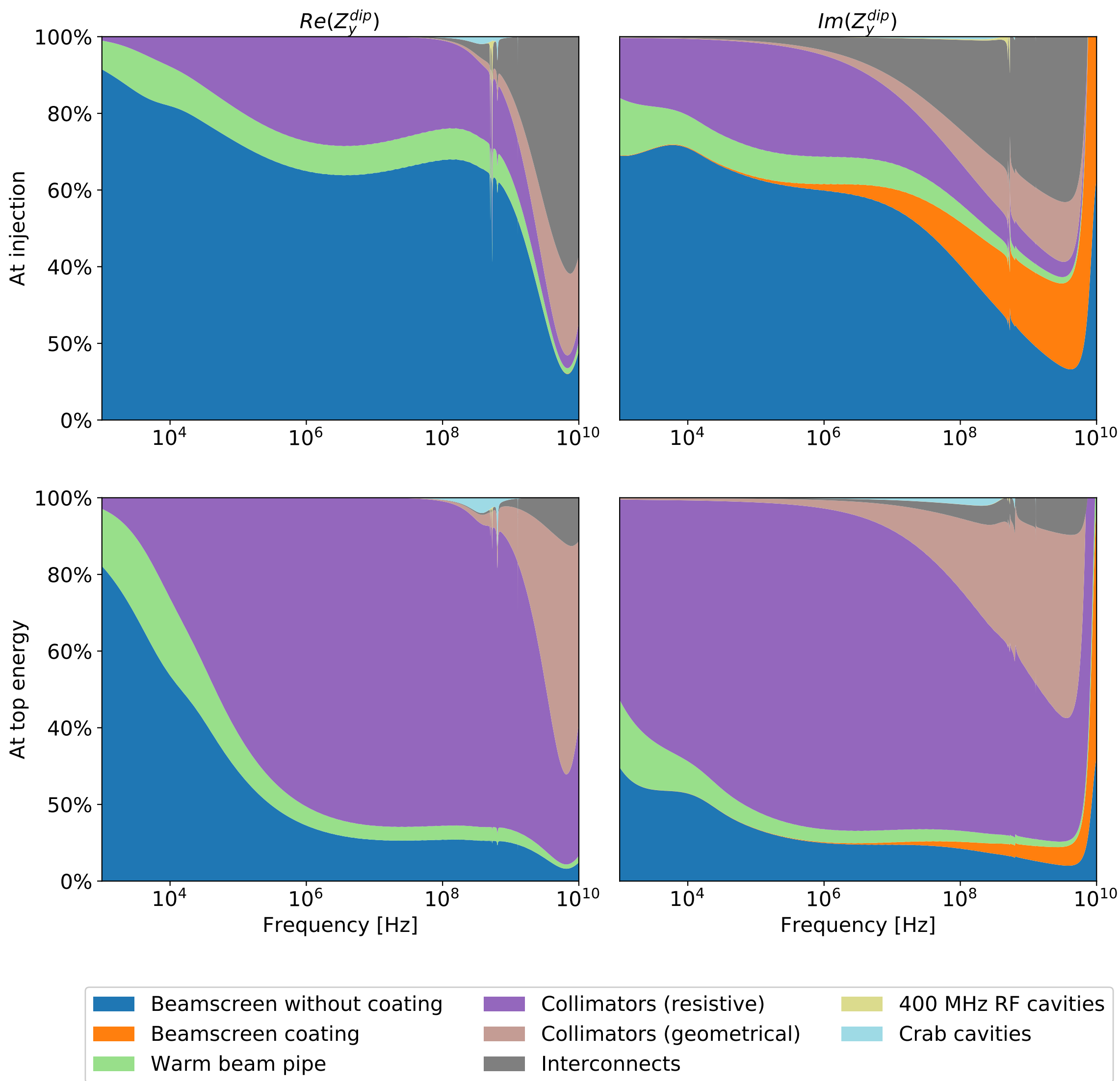

Figure 3.4: Dipolar impedance distribution by elements

In Figure 3.5 the stability regions for injection and top energy are shown for both possible polarities of the octupoles. The x-axis represents the normalized tune shift and the y-axis corresponds to the growth rate of a perturbation $-Im(\Delta\omega) = -Im(\Delta Q)\cdot\omega_0$. A mode is stable if it lies inside the region that is covered by the octupole curve. Therefore the polarity should be chosen depending on which provides the best stability.

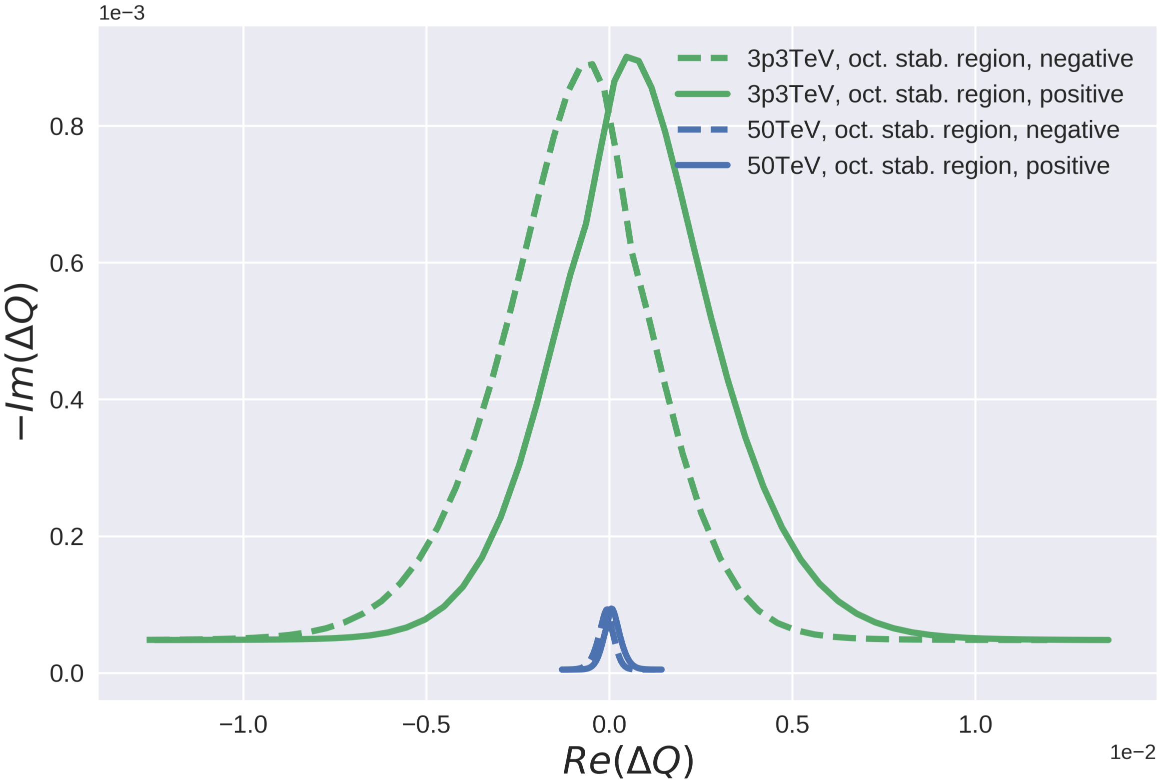

Figure 3.5: Octupole stability regions at injection and top energy

These octupole stability curves are represented by the inverse dispersion integral Equation 3.6 that was calculated with PySSD [19]. The inverse dispersion integral can be written as

$$SD^{-1} = \frac{-1}{\Delta Q_y} = \int_0^\infty \int_0^\infty \frac{J_y}{Q_y - Q_{y0}(J_x, J_y)} \frac{d\Psi}{dJ_y} dJ_x dJ_y, \tag{3.6}$$

where ΔQ_y is the complex coherent tune shift that gives the stability curve of the octupoles, Q_y is the complex coherent tune in the transverse plane, Q_{y0} is the amplitude-dependent incoherent tune in the transverse plane, Ψ represents the particle distribution, and $J_{x,y}$ are the betatron action variables [11, pp.1-4]. To calculate the stability curve the imaginary part of Q_y (which is proportional to the growth rate) is set to zero. Then one maps an interval $Re(\Delta Q_y)$ via the dispersion integral on the corresponding values of ΔQ_y. The maximum imaginary tune shift $max(Im(\Delta Q_y)_{stable})$ that is stabilized can be written as

$$max(Im(\Delta Q_y)_{stable}) \propto \underbrace{\left(\beta_{yF}^2 + \beta_{yD}^2\right) \frac{\epsilon_{norm}}{\gamma^2}}_{\text{Effectiveness}} \cdot \underbrace{O_3 \frac{I}{I_{max}} L_{oct} N_{oct}}_{\text{Strength}}, \tag{3.7}$$

where β_{yF}/β_{yD} are the betatron-functions at the location of these two families of octupoles, ϵ_{norm} is the normalized emittance, O_3 is the magnetic field gradient, I is the current

applying the magnetic field, L_{oct} is the length of one octupole, and N_{oct} is the number of octupoles.
As mentioned in the introduction and now been shown by Equation 3.7, the stability curves scale with $\frac{1}{\gamma^2}$ and are therefore a factor of about 9.6 smaller at top energy than at injection energy, although we increase the nominal current from 30 A to 720 A, as it is shown in Table 3.3.
One can obtain from Table 3.3 and Equation 3.7 that the effectiveness of the octupoles in the FCC is going to be a factor of 21.54 weaker than in the LHC. However, the strength of the FCC octupoles is a factor of 15.56 higher than in the LHC. Summed up, the FCC-hh loses 27,75 % of the overall stabilizing influence of the octupoles compared to the LHC (both at top energy). The increase in the strength is gained by longer and more octupoles but especially because of the much higher magnetic field gradient O_3. The magnetic field gradient O_3 is much higher because the octupole magnet poles can be placed much closer to the beam, due to the more compact beam screen design in the FCC-hh than in the LHC.

Parameter	LHC top energy	FCC injection/top energy
Gradient O_3 / (T/m^{-3})	63100	200 000
Length L_{oct} / (m)	0.32	0.5
Numb. of oct. N_{oct}	168	480
β_{yD} / (m)	175.5	352
β_{yF} / (m)	30.1	64
Emittance ϵ_{norm} / (m)	3.75	2.2
Max. current I_{max} / (A)	550	720
Nominal current I / (A)	500	30/720

Table 3.3: Octupole parameter for the LHC and FCC-hh [19]

3.3 Proposed transverse feedback for beam stabilization

In the LHC, the stabilization scheme of a transverse feedback system and a set of 168 octupoles sufficiently stabilizes the beam during operation. For the FCC-hh, a similar stabilization scheme is proposed with a set of 480 octupoles. It is planned that the transverse feedback system damps head-tail azimuthal mode $l = 0$ sufficiently while octupoles are used to support the transverse feedback system regarding all other modes. As it was already introduced, a mode is considered as stable if its complex coherent tune shift is located within the stability curve of the octupoles. In reality, it is common for an observed instability growth rate to be higher than the prediction. Hence, the modes should not just be under the octupole stability curve, but a safety margin of 3 should be present between the most unstable mode and the octupole stability curve. Nevertheless, one should not only consider taking the strongest possible transverse feedback setting because the uncertainties in the electronics could be amplified and would themselves excite instabilities in the beam that are not yet predictable. Due to these facts, one requires two properties for choosing a suitable transverse feedback setting. The transverse feedback setting should:

- be as low as possible to reduce instabilities caused by uncertainties in the feedback electronics
- stabilize the beam for a value of Q_p ranging from 0.0 to 20.0 providing a safety factor of at least 3.0 in combination with the passive stabilization by the octupoles

The normalized chromaticity Q_p is defined as

$$Q_p = Q_0 \cdot \xi, \tag{3.8}$$

where Q_0 is the natural tune given by the accelerator design, and ξ is the chromaticity representing the dependency of ΔQ with respect to δ.
Therefore, different feedback settings have been checked for Q_p ranging from 0.0 to 20.0 to find a transverse feedback setting that can locate all modes below the octupole stability curve. In this chapter plots of corresponding growth rate vs. chromaticity like Figure 3.6 are going to be shown to make it easier to compare, e.g., different damper gains, DELPHI and NHT or the single and multi-bunch case. One may find it surprising by how much the growth rate gets damped already for weak dampers as it is shown in Figure 3.6. This fact also initialized the requirement to validate the data with a second Vlasov solver.

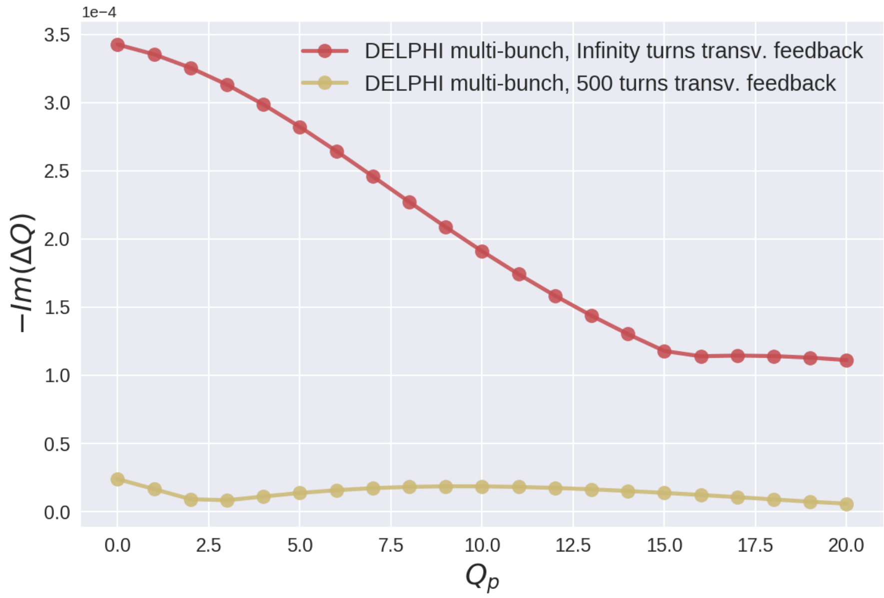

Figure 3.6: Corresponding growth rate vs. Q_p, no transverse feedback and a weak transverse feedback, multi-bunch case, top energy

3.3.1 Injection energy

The stability diagram in Figure 3.7a shows that a 60 turns transverse feedback is sufficient to stabilize the modes of the beam and provide a safety factor of **6.1/8.0** to the borders of the stability region for **positive/negative** octupole polarity. The azimuthal modes have been assigned as it has been explained in Section 3.1 and then shifted according to the azimuthal mode number l so that all modes are centered around 0.
Also head-tail azimuthal mode $l = 0$ is damped at $Q_p = 0.0$. This is important as we want the transverse feedback to damp head-tail azimuthal mode $l = 0$ and $Q_p = 0.0$ represents the worst case.
Figure 3.7b shows that head-tail azimuthal mode $l = -1$ is the most unstable mode in a Q_p range from 0.0 to 12.0. From there on, head-tail azimuthal mode $l = -2$ is going to be the most unstable. It is also shown that the instability of head-tail azimuthal mode $l = -1$ is initially excited with increasing Q_p before it gets damped.
The stability diagrams, contained in Figure 3.7, show that there is a little deviation in the tune shift between the results of DELPHI and NHT. The shape of the regime of the tune shift for the different modes with increasing Q_p is the same. Furthermore, Figure 3.8 shows that both Vlasov solvers highly agree on the instability growth rate.

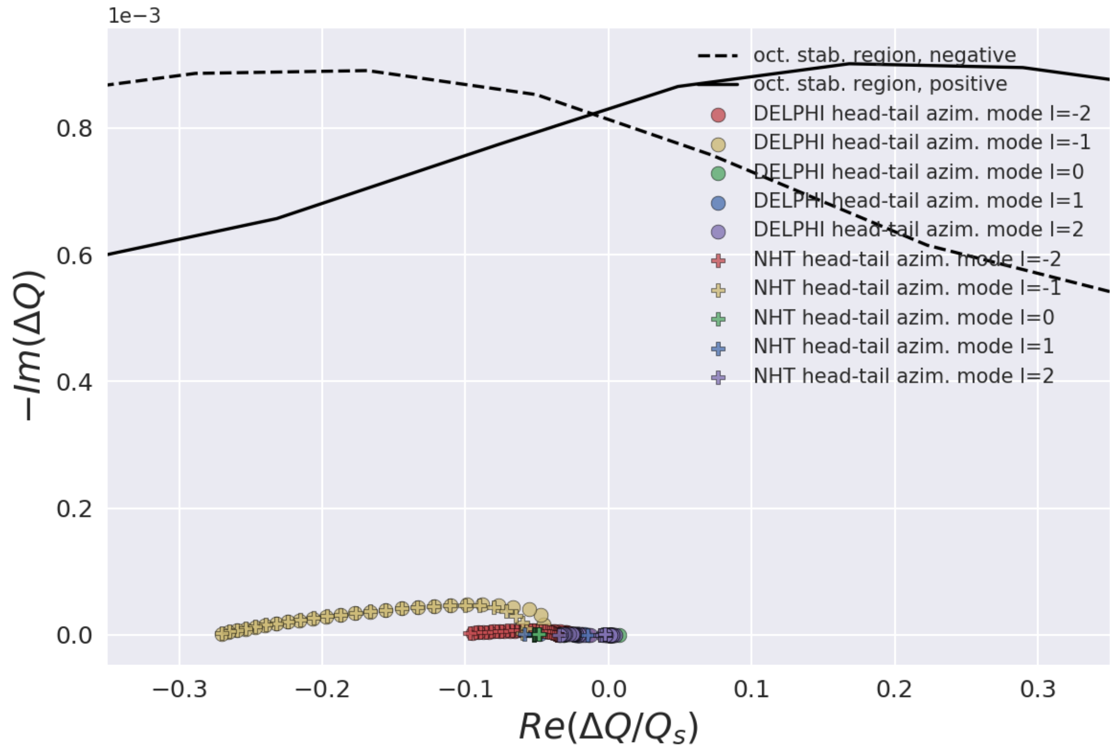

(a) Comparision of DELPHI & NHT

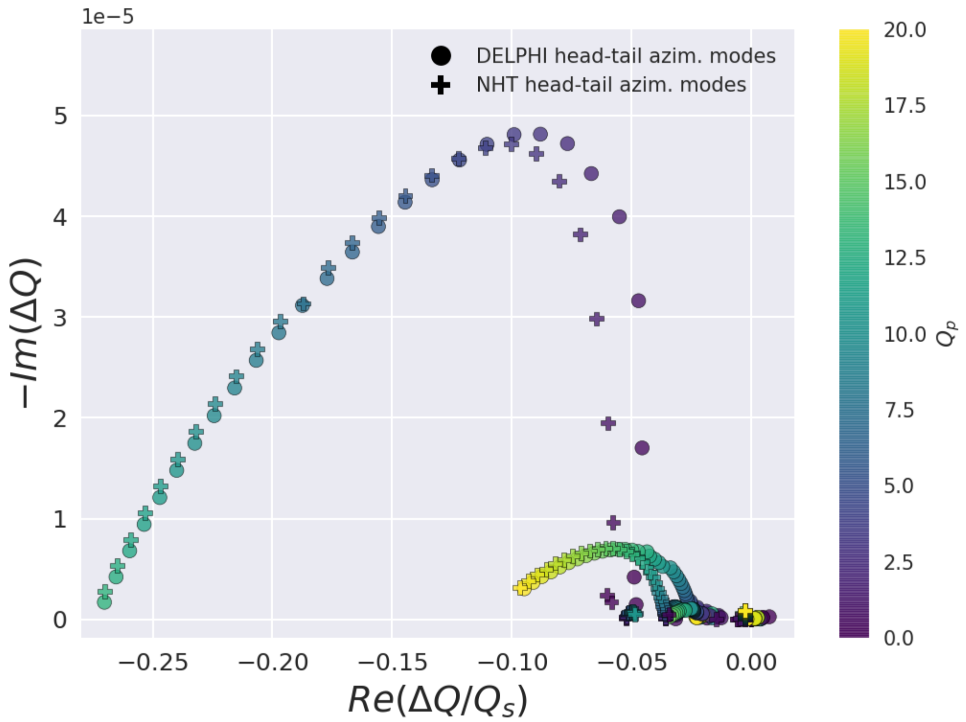

(b) Same data as in Figure 3.7a, color-coded to see evolution with Q_p

Figure 3.7: Stability diagrams, 60 turns transverse feedback, multi-bunch case, injection energy

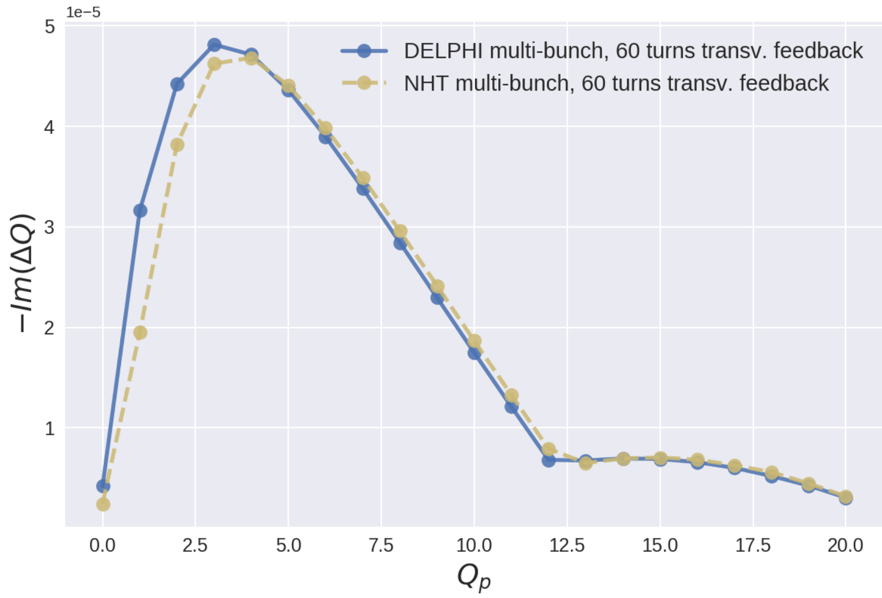

Figure 3.8: Corresponding growth rate vs. Q_p, 60 turns transverse feedback, multi-bunch case, injection energy, most unstable mode only

3.3.2 Top energy

The stability diagrams in Figure 3.9 show that a weak transverse feedback of 460 turns is sufficient to provide stability for all modes at top energy although the octupole polarity region is downscaled by a factor of about 9.6 in comparision to the region at injection energy.
The 460 turn transverse feedback provides a safety factor of **2.35/3.15** to the borders of the octupole stability region for **positive/negative** octupole polarity. Because the negative octupole polarity also gave a better safety factor at injection energy, it is proposed to set the octupoles with a negative polarity. The requirement that head-tail azimuthal mode $l = 0$ is already damped at $Q_p = 0.0$ is also satisfied.
The Figure 3.9a shows that head-tail azimuthal mode $l = -1$ is the most unstable in a region for Q_p from 0.0 to 15.5. From $Q_p = 15.5$ upward it is overtaken by head-tail azimuthal mode $l = -2$. Also, as it has been at injection energy, the growth rate for head-tail azimuthal mode $l = -1$ initially goes up before it gets damped with increasing Q_p.
Again, in the stability diagrams, in Figure 3.9, one can see that there is a little deviation in the tune shift between the results of DELPHI and NHT. The shape of the regime of the tune shift for the different modes with increasing Q_p is the same. Furthermore, Figure 3.10 shows that the both Vlasov solvers highly agree in the instability growth rate.

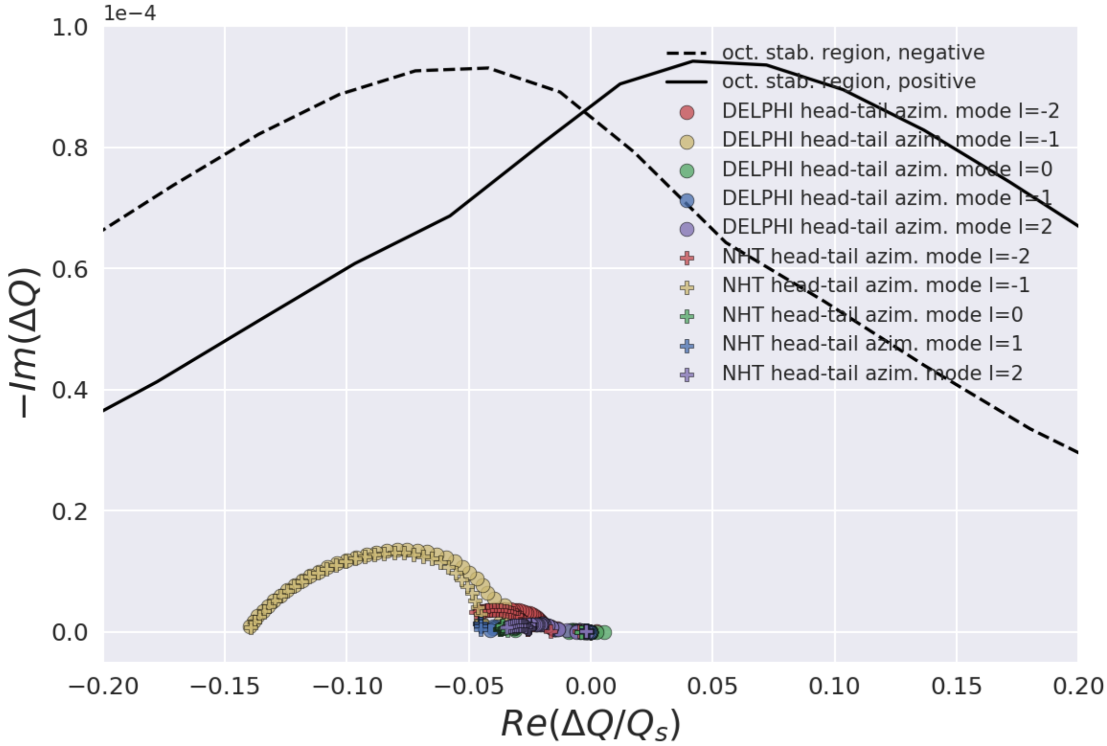

(a) Comparision of DELPHI & NHT

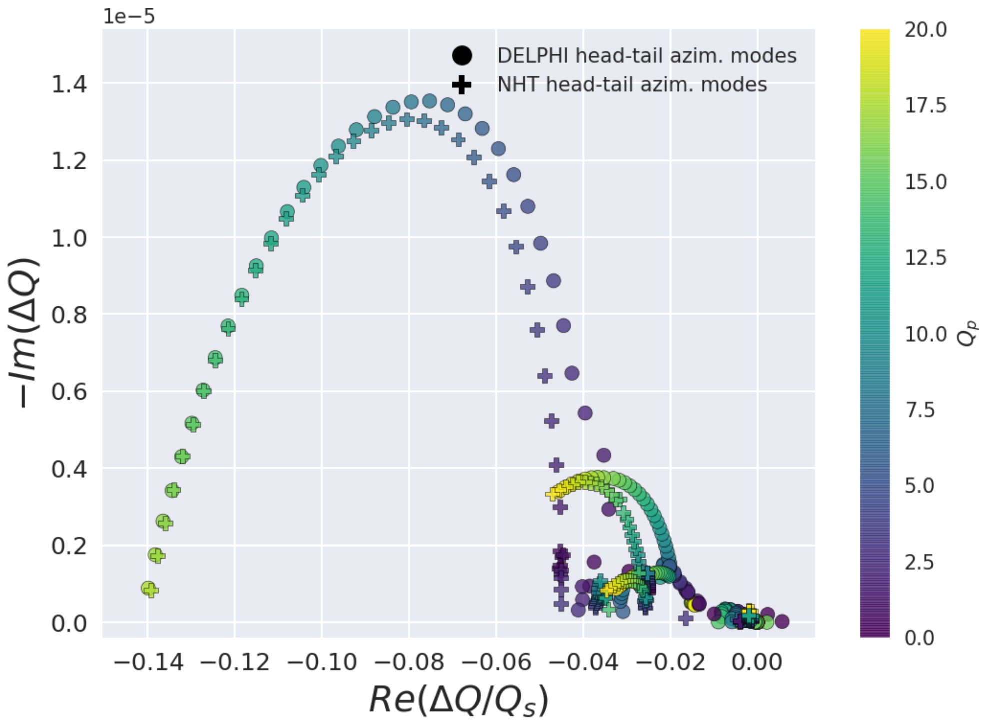

(b) Same data as in Figure 3.9a, color-coded to see evolution with Q_p

Figure 3.9: Stability diagrams, 460 turns transverse feedback, multi-buch case, top energy

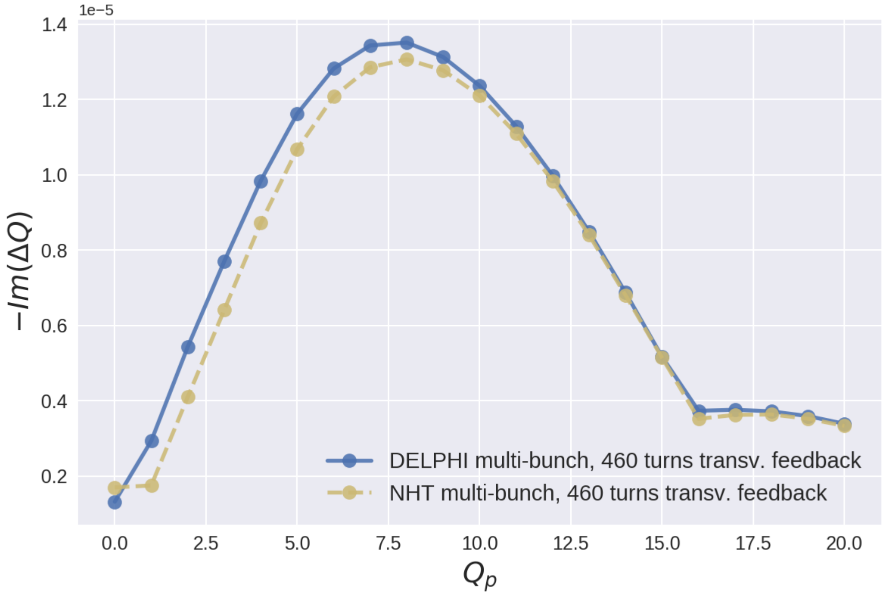

Figure 3.10: Corresponding growth rate vs. Q_p, 460 turns transverse feedback, multi-bunch case, top energy, most unstable mode only

3.4 Influence of the different higher order modes on the coupled-bunch growth rate

Higher order modes **(HOMs)** are electromagnetic modes with a higher frequency than the fundamental mode in RF cavities [3, p.27]. They are known to drive coupled-bunch-instabilities.
Figure 3.11 had been the initial spark that drew attention to the coupled-bunch growth rate and finally in the investigation of the different HOMs. It shows that the coupled-bunch growth rate is not going to be damped totally, although strong transverse feedback of 50 turns is used. There is nearly a factor of two between the single bunch and multi-bunch case. The single bunch case ignores the bunch-to-bunch interaction by putting only one bunch in the ring. A scan with an impedance without HOMs has been performed for comparison. Figure 3.12 shows that the strong transverse feedback of 50 turns can damp the growth rate down to the single bunch growth rate if no HOMs are present in the impedance. The discrepancy between the single bunch and the multi-bunch case can be a very crucial point since studies are often done for single bunch case because it is much easier to calculate and assume that strong transverse feedback will take away the coupled-bunch growth rate.
For the impedances at injection and top energy six different HOMs are given. These modes have been added to a smooth impedance (impedance without HOMs) separately for injection and top energy. These impedance models have then been simulated with Nested Head-Tail and compared to the results of a simulation for a total smooth impedance. This comparison will provide information about the influences of the different modes on the coupled-bunch growth rate.

Figure 3.11: Comparison of single and multi-bunch case for FCC-hh impedance at top energy that called attention to investigate the HOMs separatly

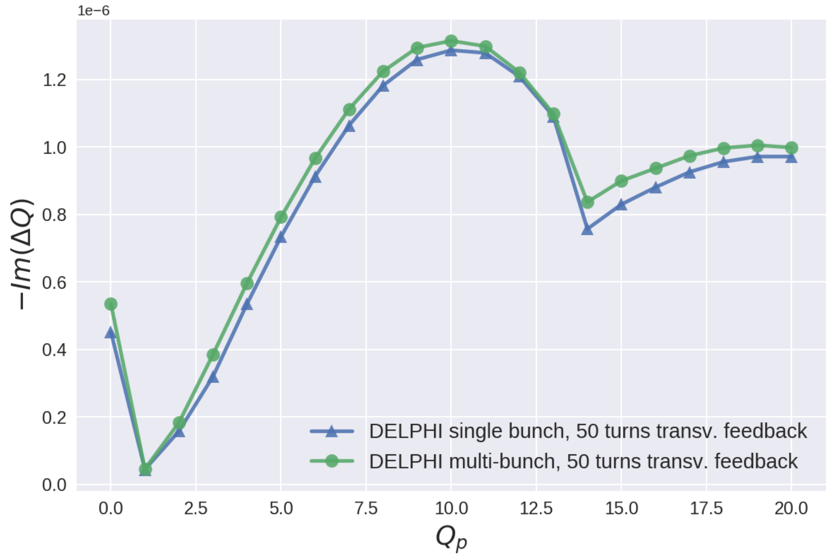

Figure 3.12: Same as Figure 3.11, but for the impedance without the HOMs

3.4.1 Injection energy

Table 3.4 shows the six different HOMs present in the impedance of the FCC-hh at injection energy. $R_\perp$ is the shunt impedance and the quality factor Q represents how long the perturbation caused by trapped electromagnetic fields persists. It can also be written as $Q = \omega U / P_{loss}$, where ω represents the angular frequency of the mode, U is the energy stored in the mode and P_{loss} is the power loss due to radiation or ohmic loses [3, p.28]. Therefore it is said that the trapped electromagnetic field from HOM number five persists for a long time and is supposed to have a significant influence on the coupled-bunch growth rate. The crab cavities cause HOM number five.

Index	Frequency / GHz	$R_\perp$ / (KOhm/m)	Q
1	0.5	653	137
2	0.534	1502	93
3	0.4	57.19	1
4	0.638	146.3	35
5	1.27	3673	23000
6	0.643	0.9595	40

Table 3.4: HOMs for injection energy impedance

Figure 3.13 shows the corresponding growth rate vs. Q_p plots for different transverse feedback settings. At injection energy, there is nearly no difference between the growth rate between a smooth impedance and one including the HOMs. Therefore it is feasible to consider the single bunch case only to approximate reality at injection energy if a strong transverse feedback is used.

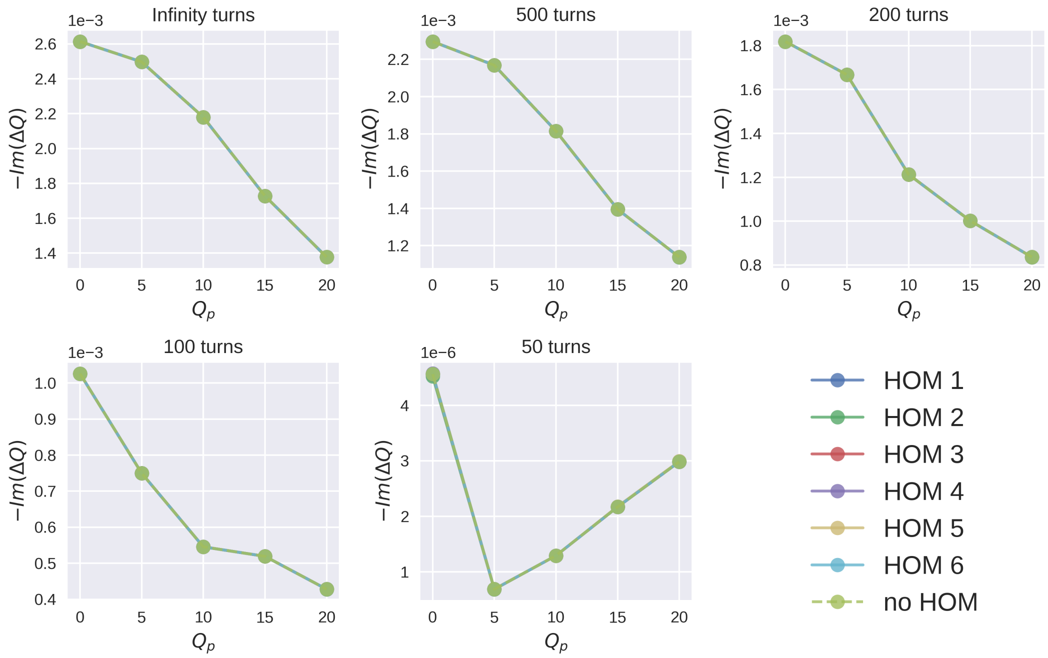

Figure 3.13: Corresponding growth rate vs. Q_p for different HOMs and transverse feedback settings at injection energy

3.4.2 Top energy

Table 3.5 shows the HOMs for the impedance at top energy. These tables differ in the shunt impedance $R_{\perp}$. HOM number five sticks out again, with an even higher shunt impedance.

Index	Frequency / GHz	$R_{\perp}$ / (KOhm/m)	Q
1	0.5	653	137
2	0.534	1502	93
3	0.4	1006	1
4	0.638	2575	35
5	1.27	64640	23000
6	0.643	15.13	40

Table 3.5: HOMs for top energy impedance

Figure 3.14 shows a corresponding growth rate vs. Q_p plots for different strong transverse feedback settings at top energy. This time, HOM number five, which is caused by the crab cavities, sticks out in the plots. It has a significant influence on the growth rate. All others influence on the growth rate is comparably neglectable.

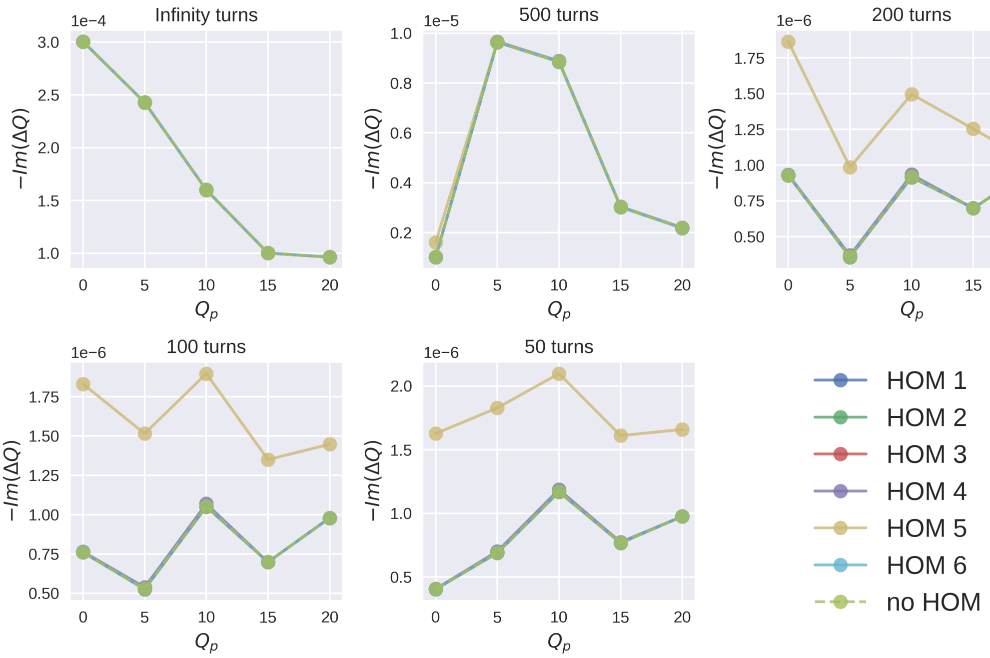

Figure 3.14: Corresponding growth rate vs. Q_p for different HOMs and transverse feedback settings at top energy

It is clear that the significant difference, shown in Figure 3.11 and Figure 3.12, have been caused by the HOM from the crab cavities. At injection energy, the crab cavities have a low β-function and hence nearly no influence on the coupled-bunch growth rate. Hence one may consider taking action to damp this HOM.

3.5 Destabilizing effect of strong resistive transverse feedback

In the LHC during Run 1 and Run 2, something non-intuitive concerning the stabilization by the transverse feedback system was observed. At a chromaticity around 0.0, the active transverse feedback system destabilized the beam. Therefore Elias Métral studied this destabilizing effect of strong dampers with the two Vlasov solvers GALACTIC and DELPHI for the LHC impedance and single bunch case [13].
In our studies, this effect has been discovered as well for the single bunch case as well for the multi-bunch case at top energy. The growth rate vs. Q_p plots, contained in Figure 3.15, show that transverse feedback of 200 turns provides more stability than it is provided with 50 turns transverse feedback.

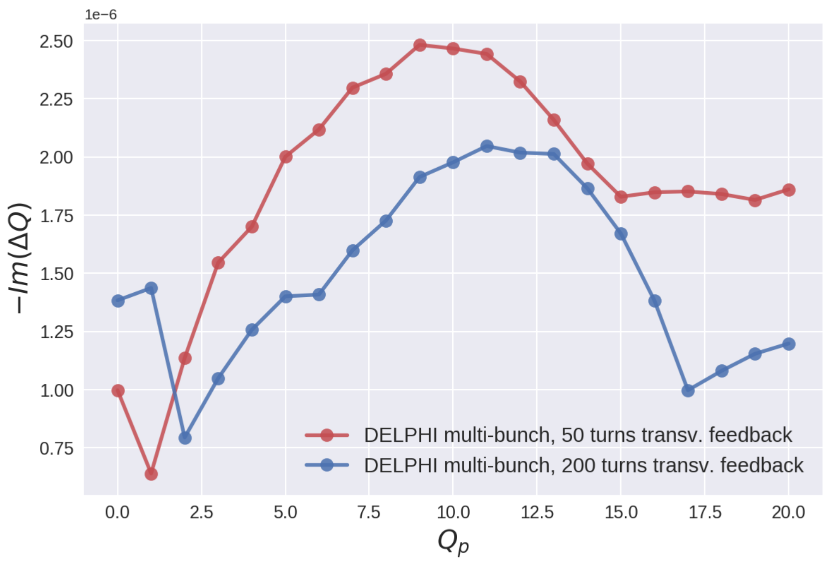

(a) Multi-bunch

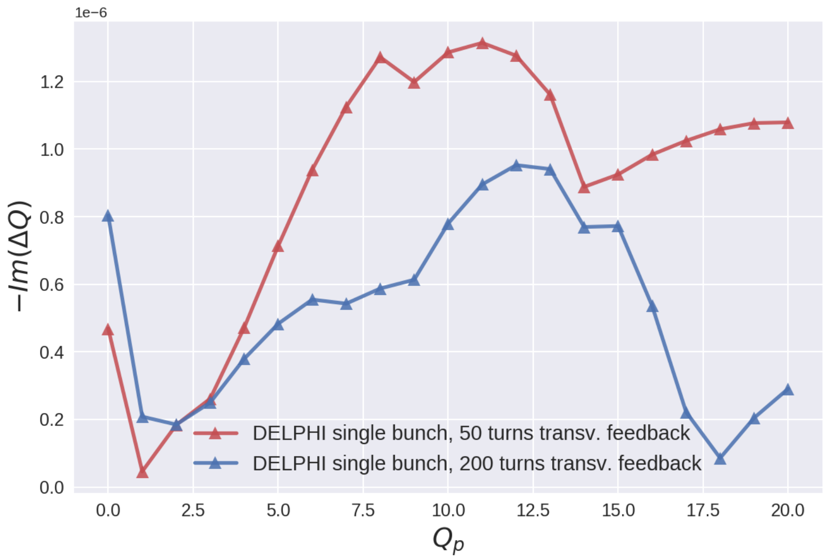

(b) Single bunch

Figure 3.15: Corresponding growth rate vs. Q_p plots comparing two strong feedback settings, single and multi-bunch case, top energy

3.6 Comparison to analytically solved Sacherer formalism for no transverse feedback

It is possible to calculate the complex coherent tune shift for every head-tail azimuthal mode l analytically with the Sacherer formalism, for the case without transverse feedback, as given in Equation 3.9.

$$\Delta Q_l = \frac{1}{1+|l|}\frac{j}{2\omega_\beta\omega_0}\frac{e\beta}{\gamma m_0}\frac{I_0}{L}\frac{\sum_P Z(\omega_p)h_l(\omega_P-\omega_\xi)}{\sum_P h_l(\omega_P-\omega_\xi)} \tag{3.9}$$

Eq. 3.9 Sacherer formalism [17]

In Equation 3.9, I_0 is the bunch current, L is the bunch length, β is defined by $\beta = v/c$, γ is the relativistic factor, ω_b is the betatron frequency, ω_0 is the revolution frequency, m_0 is the rest mass, Z is the dipolar transverse impedance, $\omega_\xi = \xi Q\omega_0/\eta$ is the chromatic angular frequency shift, η is the slippage factor, Q is the betatron tune, ω_0 is the revolution frequency of the particle, and h_l is the mode power spectrum.
One can compare the results from the Sacherer formalism to the computational approaches and analyze if there are differences and what might have caused them. The stability diagrams for injection energy in Figure 3.16 show a significant discrepancy between the computational approaches and the Sacherer formalism. The computational approaches thereby expect first of all substantial more growth rates, and second, the computational approaches predict different modes to be the most unstable. At injection and top energy, the positive and negative azimuthal mode pairs show asymmetrical behavior. Asymmetrical means in this case that the azimuthal mode pairs do not match in their complex coherent tune shifts. This asymmetry does not exist in the Sacherer formalism. All azimuthal mode pairs are symmetrical and rotate in different directions in the synchrotron phase space.
One may wonder why asymmetrical behavior in the azimuthal modes of the FCC-hh exists. The nominal bunch intensity of the FCC-hh is already in the region of mode coupling that causes non-linear effects. These non-linear effects are not taken into account in the Sacherer formalism [10, p.149]. To study this more in detail, an intensity scan has been executed with DELPHI. The plots of normalized tune shift/corresponding growth rate vs. number of particles, contained in Figure 3.18a, show the most unstable mode in red. In this plot, the integer on the y-axis defines the different head-tail azimuthal modes l. Because there is no need to separate the azimuthal modes, the different radial modes are preserved. Here $Q_p = 20.0$ is shown because the effects that are now going to be reviewed are initially clearly visible at a $Q_p = 15.0$ and become stronger with increasing Q_p. There are some mode coupling processes visible at injection and top energy between head-tail azimuthal mode $l = 0$ and head-tail azimuthal mode $l = -1$. It is furthermore interesting to see how the growth rate ascends nonlinearly in the area of the nominal beam intensity of 10^{11} for injection energy. The same effect is even more pronounced at top energy where the slope of the growth rate increases nonlinearly up to four times of the nominal bunch intensity. Furthermore, discontinuity in the slope is visible at three times the nominal bunch intensity. Thus, it seems that the mode coupling process at top energy is not as intense for nominal bunch intensity as at injection energy. This might be the reason why Figure 3.17 shows less disagreement with Sacherer than Figure 3.16. A scan, shown in Figure 3.19, with half bunch intensity for injection energy confirms this assumption, showing amended agreement with the Sacherer formalism.

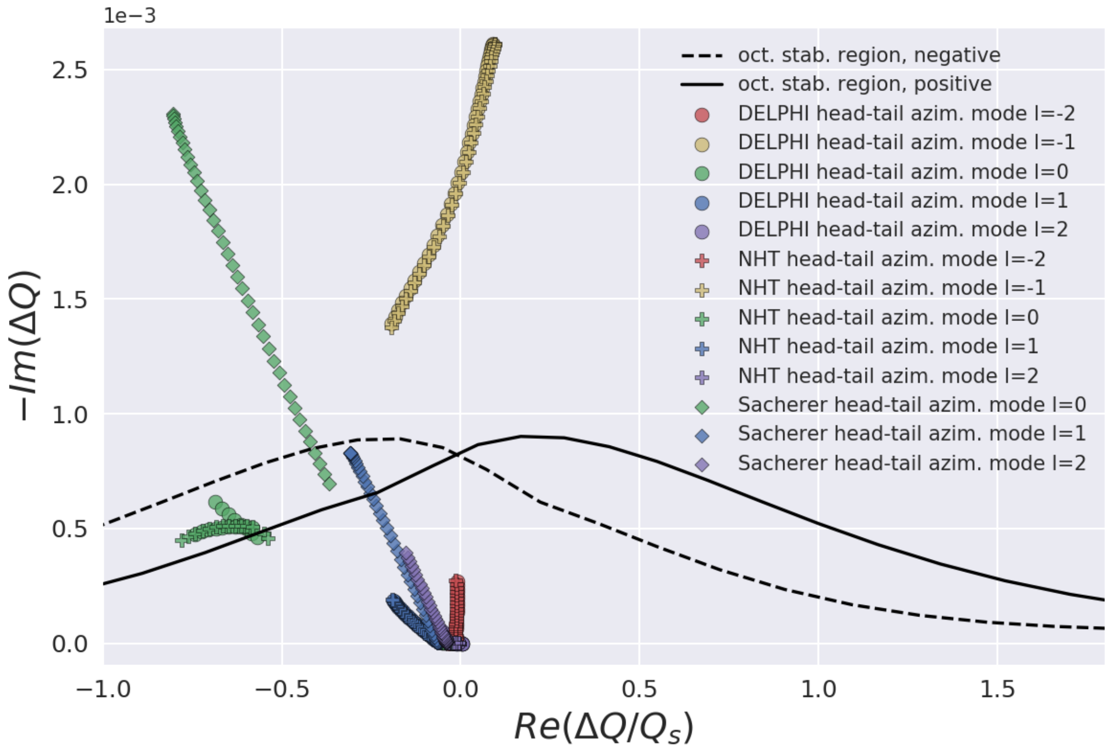

(a) Comparison of computational approaches and Sacherer formalism

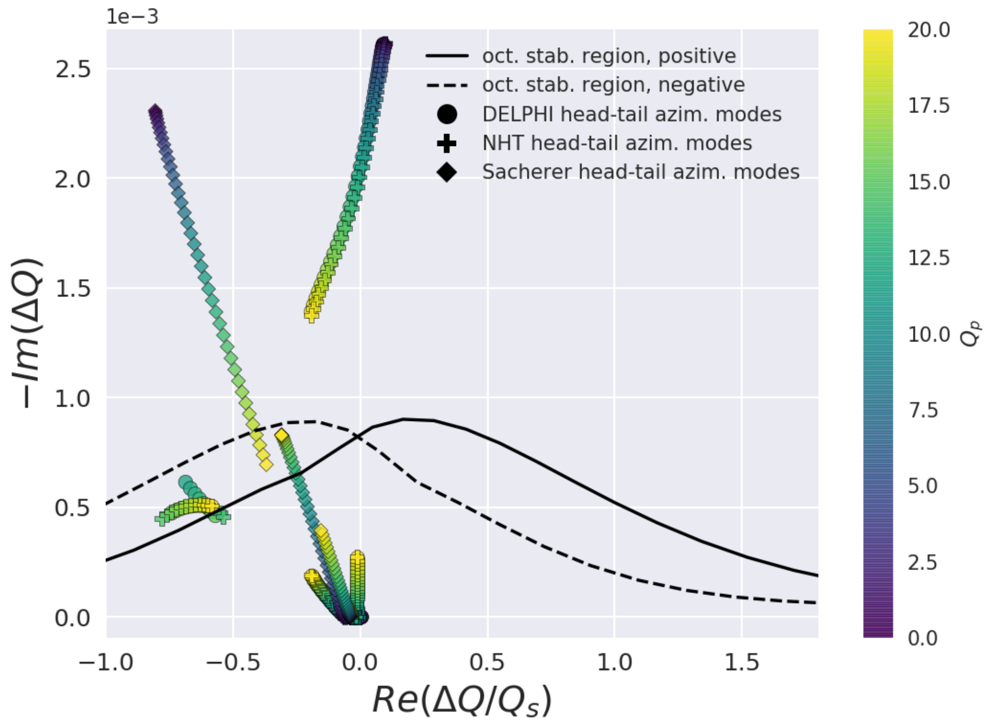

(b) Same data as in Figure 3.16a, color-coded to see evolution with Q_p

Figure 3.16: Stability diagrams, no transverse feedback, multi-bunch case, injection energy

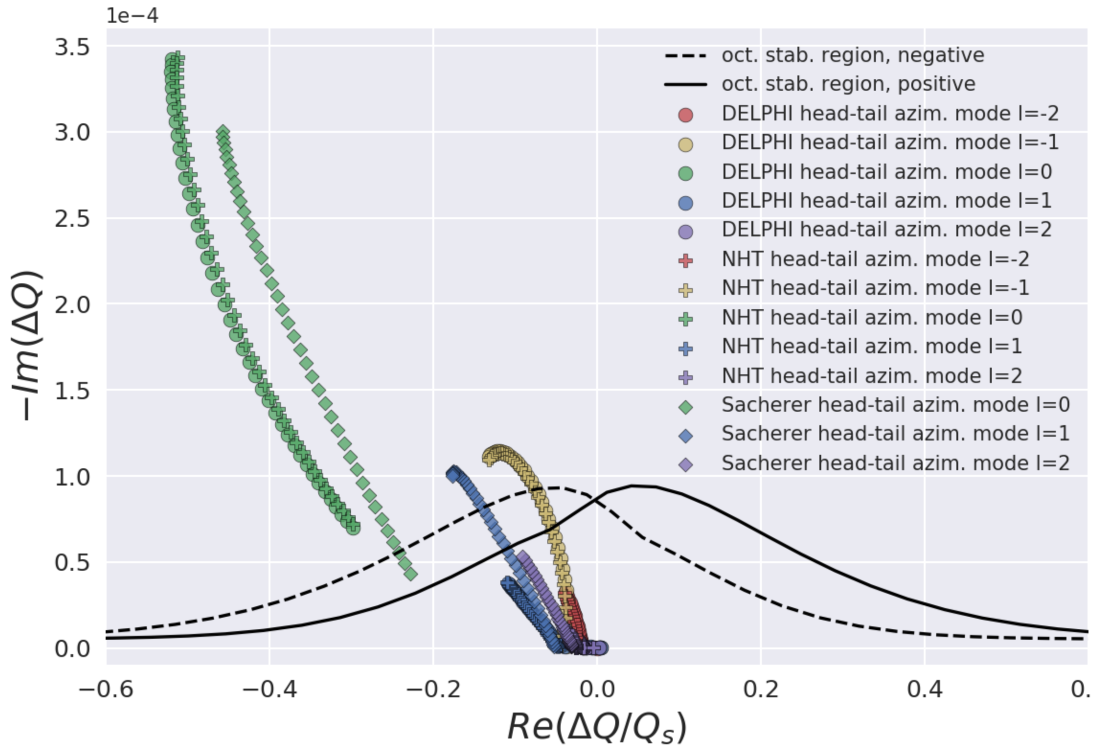

(a) Comparison of computational approaches and Sacherer formalism

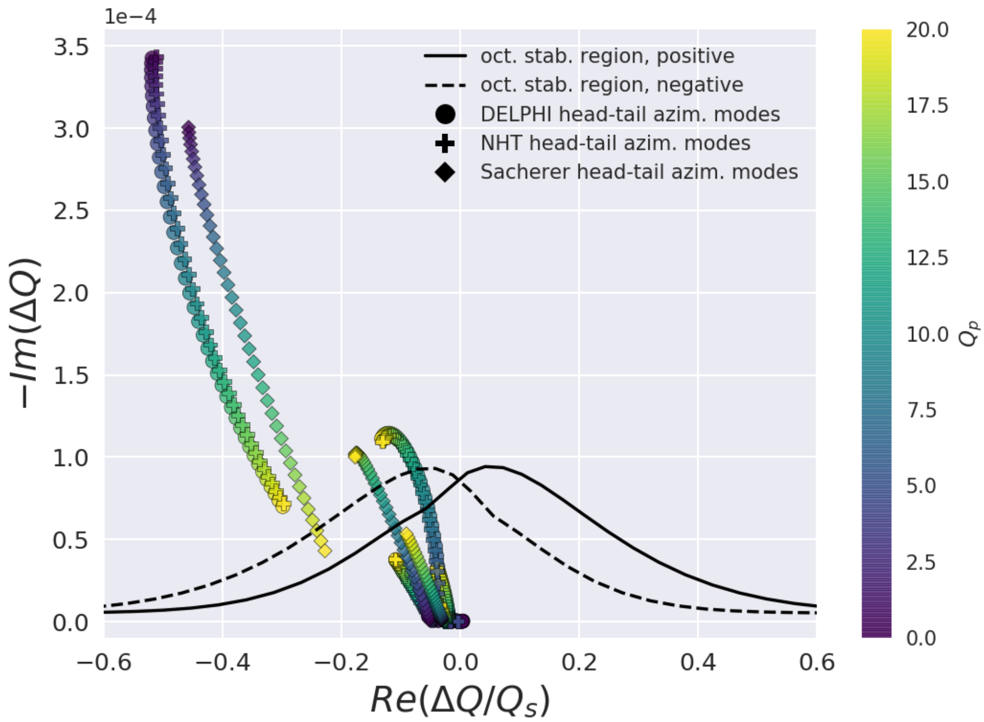

(b) Same data as in Figure 3.17a, color-coded to see evolution with Q_p

Figure 3.17: Stability diagrams, no transverse feedback, multi-buch case, top energy

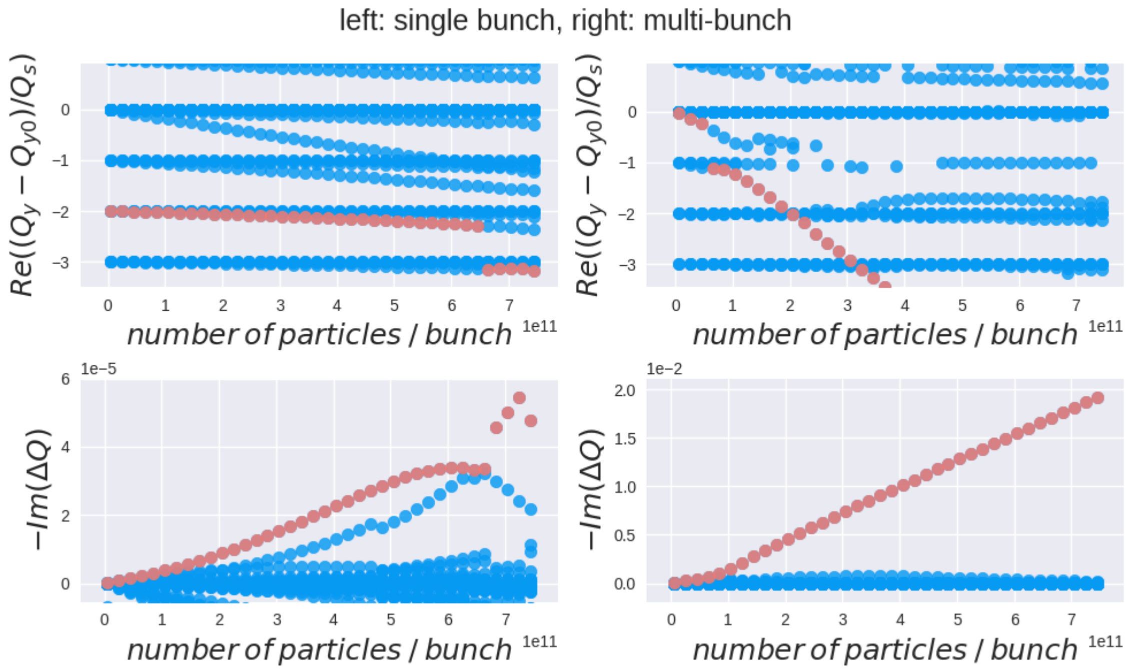

(a) Injection energy

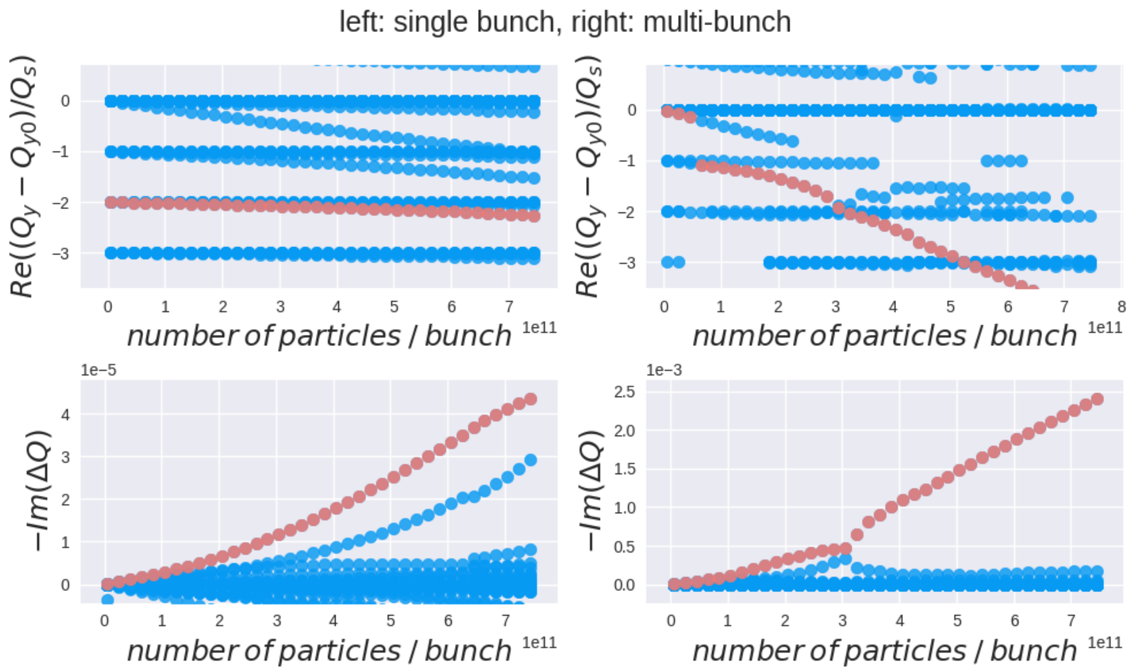

(b) Top energy

Figure 3.18: Intensity scan for $Q_p = 20.0$, no transverse feedback, multi-bunch case, injection and top energy

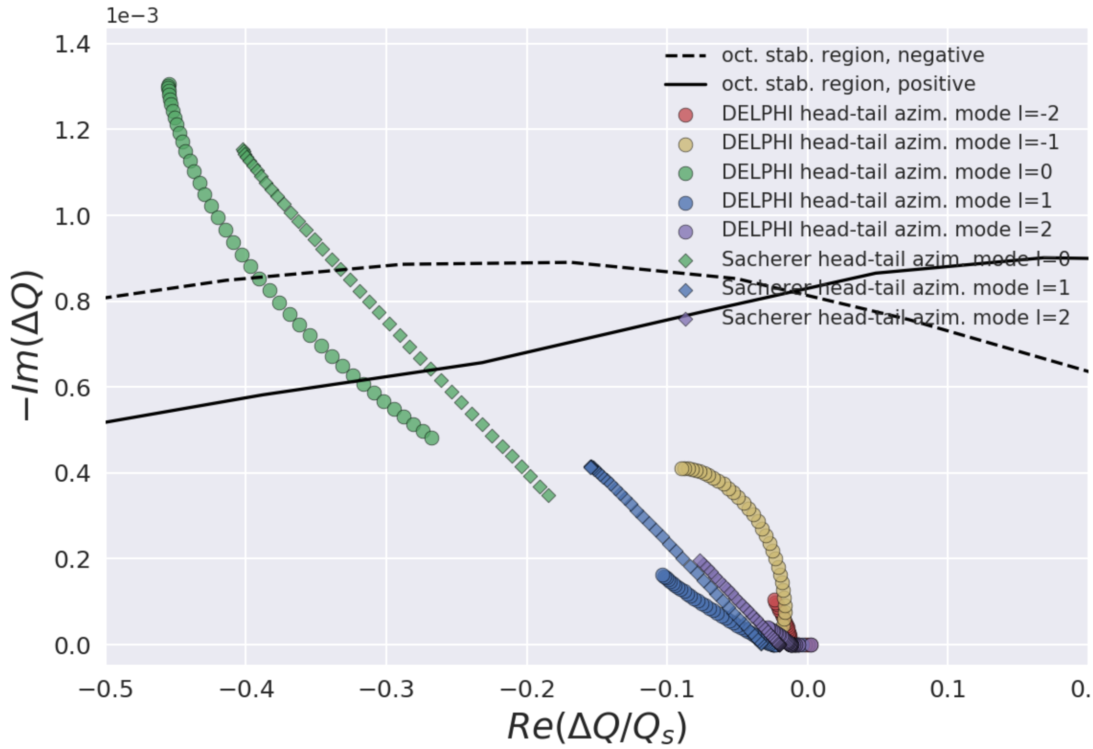

(a) Comparison of computational approaches and Sacherer formalism

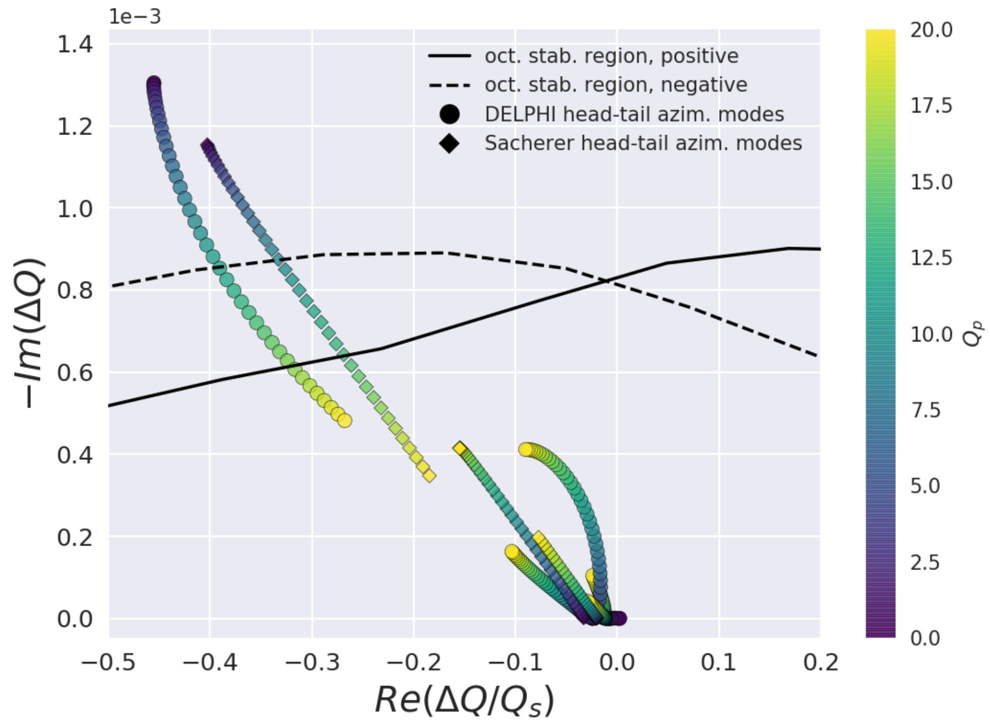

(b) Same data as in Figure 3.19a, color-coded to see evolution with Q_p

Figure 3.19: Stability diagrams, no transverse feedback, multi-bunch case, injection energy, half bunch intensity

3.7 Impedance update

In Section 3.4 it was revealed that the HOM, caused by the crab cavities, has a significant impact on the coupled-bunch growth rate. Therefore it has been proposed to damp this HOM. This proposal was accepted while this study has been performed. Hence a new impedance was exposed where the HOM caused by the crab cavities are damped. Furthermore, the impedance of the beam-screen has been reduced. These changes motivated the reinvestigation of the simulations for the proposed transverse feedback settings.
Tables 3.6 and 3.7 show the HOMs for the adapted impedance. With the improved impedance, a 60 turns transverse feedback nearly stabilizes all modes without the octupoles. Since it was claimed not to take the strongest transverse feedback possible (uncertainties in the electronics could excite instabilities) a 65 turns damper is now proposed for injection energy. The stability diagram for the 65 turns transverse feedback is shown in Figure 3.20. For top energy, the 460 turns damper is still suitable as Figure 3.21 shows. The safety factor for injection energy is still **8.0**, and for top energy, it improves to **4.0**. Both values apply to negative octupole polarity that still shows the best stabilizing effect.

Index	Frequency / GHz	$R_\perp$ / (KOhm/m)	Q
1	0.5	653	137
2	0.534	1502	93
3	0.4	57.36	1
4	0.6383	146.3	35
5	1.276	175.7	1100
6	0.6438	0.8595	40

Table 3.6: HOMs for updated injection energy impedance

Index	Frequency / GHz	$R_\perp$ / (KOhm/m)	Q
1	0.5	653	137
2	0.534	1502	93
3	0.4	1009	1
4	0.638	2575	35
5	1.27	3092	1100
6	0.643	15.13	40

Table 3.7: HOMs for updated top energy impedance

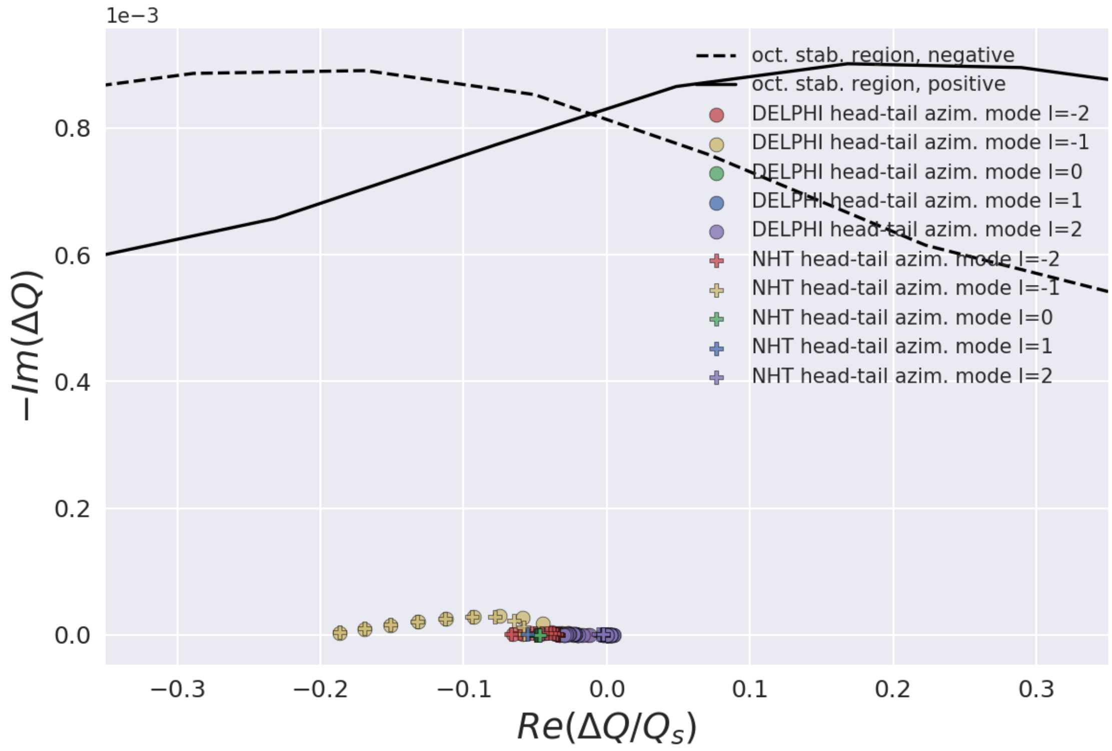

(a) Injection energy, 65 turns transverse feedback

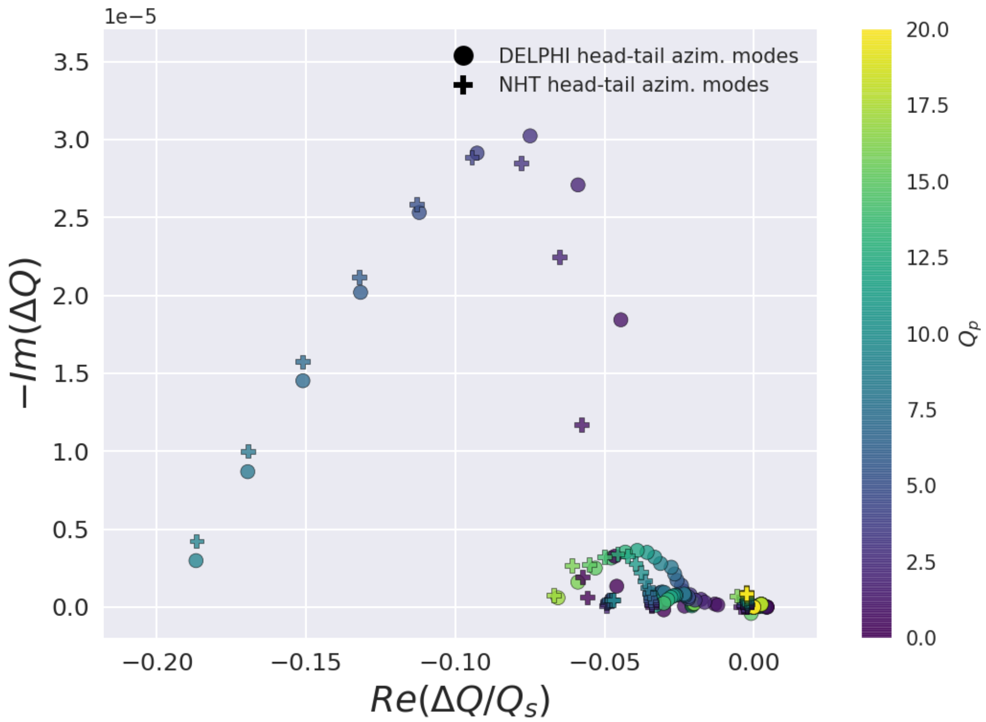

(b) Same data as in Figure 3.20a, color-coded to see evolution with Q_p

Figure 3.20: Stability diagrams after the impedance update, 65 turns transverse feedback, multi-bunch-case, injection energy

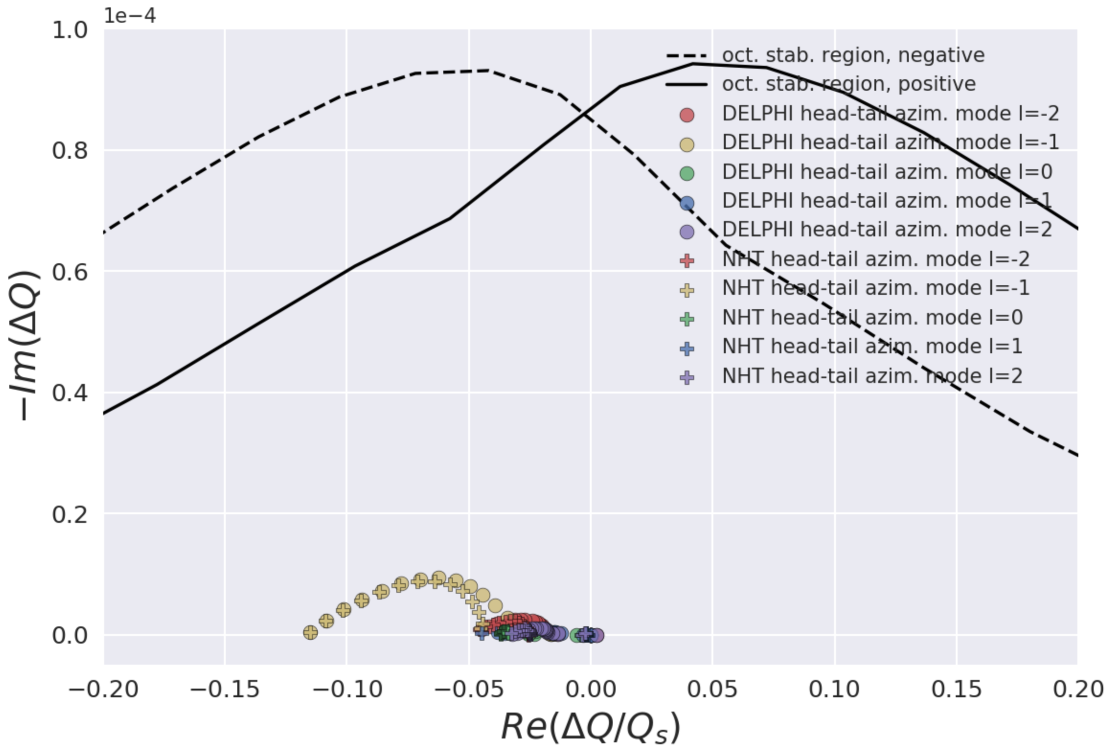

(a) Comparision of DELPHI & NHT

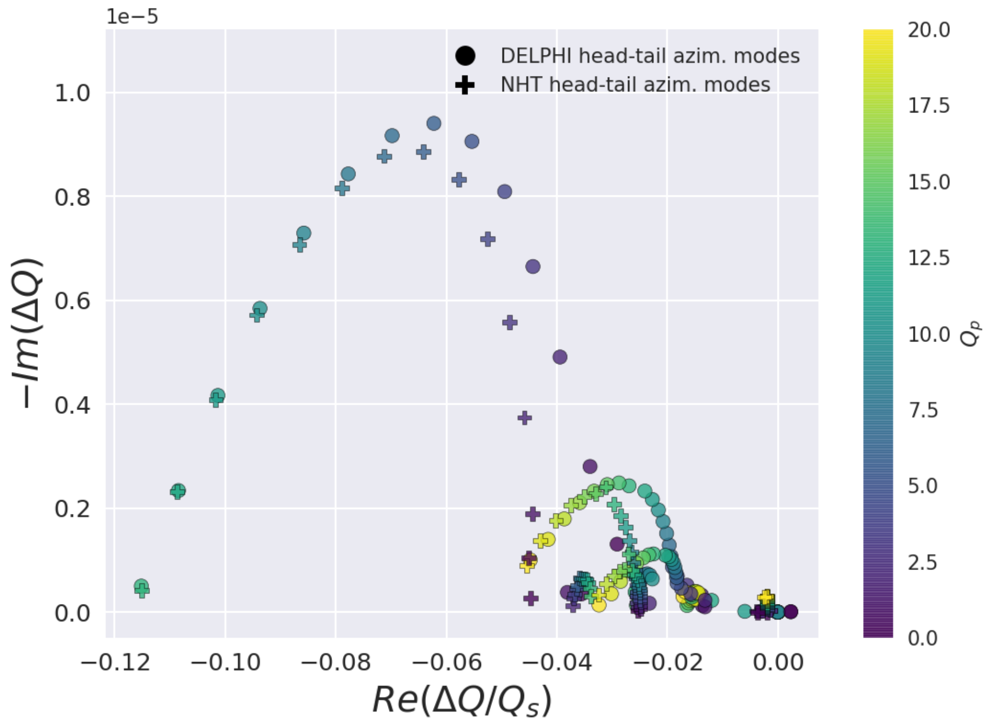

(b) Same data as in Figure 3.21a, color-coded to see evolution with Q_p

Figure 3.21: Stability diagrams after the impedance update, 460 turns transverse feedback, multi-bunch-case, top energy

Conclusion

This study analyzed and answered important stability issues for the latest available impedance, taking into account the most crucial parts of the accelerator. It was shown that the octupoles are capable of stabilizing the beam in cooperation with a transverse feedback damping rate of

- 60 turns for injection energy with a safety factor of 8.0
- 460 turns for top energy with a safety factor of 3.15.

A negative octupole polarity was proposed because it provides a better stabilization at injection and top energy.

It was revealed that the HOM (caused by the crab cavities) makes the stabilization of the coupled-bunch growth rate by the transverse feedback system more difficult.

A destabilizing effect for strong resistive transverse feedback at top energy has also been detected and shown for the single and multi-bunch case.

A comparison for no transverse feedback between two computational Vlasov solvers and the Sacherer formalism was performed. A discrepancy between them leads to a deeper analysis where it was revealed that the high bunch intensity causes mode coupling. Therefore, non-linear effects occur that the Sacherer formalism does not take into account.

The recent discovery of the crab cavity HOM having a negative impact, lead to an impedance update. For this impedance, which is now available at the impedance database, a transverse feedback damping rate has been proposed of

- 65 turns for injection energy with a safety factor of 8.0
- 460 turns for top energy with a safety factor of 4.0

to provide sufficient stabilization of all modes.

In the introduction, it was mentioned that the transverse beam stability is an important aspect of the proof-of-concept for the CDR of the FCC-hh. In this study, it was shown that the planned stabilization scheme of transverse feedback with octupoles is capable of providing the required transverse beam stability and is, therefore, mentioned in the CDR.

Bibliography

[1] David Amorim. “Hadron collective effects studies for the LHC and FCC-hh project”. MA thesis. Grenoble INP-PHELMA, 2016.

[2] Sergey Arsenyev. *FCC-hh impedance*. 2018. URL: https://impedance.web.cern.ch/impedance/fcchh/impedances.html.

[3] Sergey Arsenyev. “Photonic Band Gap Structures for Superconducting Radio-frequency Particle Accelerators”. PhD thesis. Massachusetts Institute of Technology, 2016.

[4] Simon Baird. “Accelerators for pedestrians”. In: *CERN Document Server* (Feb. 2007).

[5] Ryan Bodenstein. “A Procedure for Beamline Characterization and Tuning in Open-Ended Beamlines”. PhD thesis. University of Virginia, 2012.

[6] Ryan Bodenstein. *Lecture 10, Beams and Imperfections, John Adams Institute for Accelerator Science, University of Oxford*. 2016. URL: https://indico.cern.ch/event/668489/sessions/251711/#20171102.

[7] Alexey Burov. “Nested Head-Tail Vlasov Solver”. In: *arXiv* (Aug. 2013).

[8] Antoine Chance et al. “OVERVIEW OF ARC OPTICS OF FCC-h”. In: *Proceedings of IPAC 2018, MOPMF025, A01 Hadron Colliders* (2018).

[9] Alexander Wu Chao. *Physics of collective beam instabilities in high energy accelerators*. New York: John Wiley & Sons Inc., 1993.

[10] Yong Ho Chin. “2.13 Head-Tail and Transverse Mode-Coupling Instabilities”. In: *ICFA Beam Dynamics Newsletter* 69 (2016), pp. 142–150.

[11] Jacques Gareyte, Jean-Pierre Koutchouk, and F Ruggiero. *Landau damping dynamic aperture and octupole in LHC*. Tech. rep. LHC-Project-Report-91. CERN-LHC-Project-Report-91. revised version number 1 submitted on 2003-08-21 14:12:02. Geneva: CERN, Feb. 1997. URL: https://cds.cern.ch/record/321824.

[12] Wolfgang Hofle. *The LHC Transverse Feedback System and Persepectives for FCC-hh*. 2016. URL: https://indico.cern.ch/event/669849/contributions/2748421/attachments/1537851/2410228/EuroCircle_.pdf.

[13] Elias Métral et al. “Destabilizing Effect of the LHC Transverse Damper”. In: *Proceedings of IPAC 2018, THPAF048, D05 Coherent and Incoherent Instabilities - Theory, Simulations, Code Developments* (2018).

[14] Frank Zimmermann Mikahel Benedikt. “FCC: COLLIDERS AT THE ENERGY FRONTIER”. In: *Proceedings of IPAC 2018, THYGBD1, A16 Advanced Concepts* (2018).

[15] Nicolas Mounet. *DELPHI: an analytic Vlasov Solver for impedance-drive modes, CERN presentation slides*. Apr. 2014. URL: https://espace.cern.ch/be-dep-workspace/abp/HSC/Meetings/DELPHI-expanded.pdf.

[16] CERN - Council - S/106. “European Strategy Session of Council”. In: (May 2013).

[17] Frank Sacherer. “Transverse bunched beam instabilities”. In: *CERN Document Server* (1974).

[18] Oliver Boine-Frankenheim Sergey Arsenyev Daniel Schulte. “FCC-hh Transverse Impedance Budget”. In: *Proceedings of IPAC 2018, MOPMF029, A01 Hadron Colliders* (2018).

[19] Claudia Tambasco et al. “Landau Damping Studies for the FCC: Octupole Magnets, Electron Lens and Beam-Beam Effects”. In: *Proceedings of IPAC 2018, THPAF074, 05 Beam Dynamics and EM Fields* (2018).

[20] E. Wilson. *Cern Accelerator School Vol. 1 - Non-Linearities and Resonances*. 1994.

[21] Andrzej Wolski. *Beam Dynamics in High Energy Particle Accelerators*. Imperial College Press, 2047.